Nano Today 27 (2019) 120–145

Contents lists available at ScienceDirect

Nano Today

journal homepage: www.elsevier.com/locate/nanotoday

Review

# The fast and the furious: Ultrafast hot electrons in plasmonic metastructures. Size and structure matter

Lucas V. Besteiro[a,b], Peng Yu[a], Zhiming Wang[a,*], Alexander W. Holleitner[c,*], Gregory V. Hartland[d], Gary P. Wiederrecht[e], Alexander O. Govorov[a,f,*]

[a] Institute of Fundamental and Frontier Sciences, University of Electronic Science and Technology of China, Chengdu, 610054, China
[b] Centre Énergie Matériaux et Télécommunications, Institut National de la Recherche Scientifique, Varennes, Québec, J3X 1S2, Canada
[c] Walter Schottky Institute and Physics Department, Technical University of Munich, 85748, Garching, Germany
[d] Department of Chemistry and Biochemistry, University of Notre Dame, Notre Dame, IN, 46556-5670, USA
[e] Center for Nanoscale Materials, Argonne National Laboratory, Lemont, IL, 60439, USA
[f] Department of Physics and Astronomy, Ohio University, Athens, OH, 45701, USA

ARTICLE INFO

*Article history:*
Received 1 March 2019
Received in revised form 28 April 2019
Accepted 21 May 2019
Available online 18 July 2019

*Keywords:*
Plasmonic
Hot electrons
Photocatalysis
Theory
Quantum two-temperature model
Time-resolved spectroscopy
Photoemission
Nanoparticles
Metamaterials
Metamaterial absorber
Breathing modes
Vibrational modes
Acoustic modes

ABSTRACT

This review focuses on the generation of energetic (hot) electrons in plasmonic metastructures and nanomaterials, and their characterization through time-resolved spectroscopy. Excitation of hot electrons under illumination occurs in any metal or conductor, but their number will vary for each type of nanostructure. While plasmonic resonances are well described classically, the excitation of hot electrons (HEs) is a quantum process and its description requires further elaboration. Some potential applications for HEs lie in the fields of photo-catalysis and optoelectronics, and their study constitutes a very active interdisciplinary research direction that involves chemistry, physics and device engineering. Here we focus on some particular developments enabling the use of hot carriers for these applications. Particularly, we discuss the approaches and structures required to create hot carriers, the temporal dynamics of hot carrier formation and relaxation, and relevant theoretical methods used to compute the HE dynamics.

The observations presented here support the conclusion that the shape of the nanostructure matters. Although metastructures with infrared gap plasmons can exhibit spatially extended hot spots and anomalously large numbers of non-thermalized HEs, most excited carriers in a plasmonic nanostructure typically have small excitation energies. Here we discuss ways to strongly increase the number of high-energy electrons, highlighting the role of hot spots, system size, geometry and resonant frequencies. To generate HEs efficiently, we can take advantage of special geometries with hot spots, such as metamaterial absorbers with ultra-narrow gaps or nanostars. Furthermore, we discuss the applications in ultrafast electronics based on plasmon-enhanced photoemission and tunneling in the nonlinear regime. Considering the longer timescale phenomena, we also present studies on the coherent dynamics in a nanostructure after electron thermalization, showing acoustic breathing modes. In this paper, we review some key developments in the field of ultra-fast plasmonic dynamics and provide a perspective for its possible next steps.



**Contents**



* Corresponding authors.
*E-mail addresses:* zhmwang@uestc.edu.cn (Z. Wang), holleitner@wsi.tum.de (A.W. Holleitner), govorov@ohio.edu (A.O. Govorov).

https://doi.org/10.1016/j.nantod.2019.05.006
1748-0132/

## Introduction

The dynamical properties of conductive materials are fundamentally different to those of molecules and semiconductors. Of course, this arises from the fundamentally different structures of the electronic quantum states in these materials (Fig. 1) [1]. Importantly, the quantum electronic structure of a material dictates its behavior and practical applications (Fig. 1) [1,2]. Although arising from different reasons, both molecules and semiconductors have an energy gap of quantum origin, which separates occupied and unoccupied states, and related optical inter-level transitions (Fig. 1a,b); in the case of semiconductors, the excitation of an electron across this gap creates an interacting electron-hole pair known as an exciton. Analogously to what occurs with the state separation in molecular fluorophores, excitons and inter-band transitions govern the optical properties of a semiconductor, providing the possibility of designing optical emitters, lasers and detectors. In contrast, a conductive material is gapless and the main excitations produced by light in this case are classical and called plasmons [3]. Metals are widely used in radiophysics and optoelectronics as contacts, antennas and optical mirrors [4]. When a metal is small in size or is nanostructured, it exhibits very strong optical resonances, which are directly observed via the absorption and scattering of light [5,6]. These optical resonances, i.e. plasmons confined into a small volume, are attracting lots of interest due to their unique properties that can potentially be used in sensors, ultra-small waveguides, energy-conversion elements, photo-chemical reactors, etc. Plasmonics is presently a very broad and active field, with thousands of papers published every year. Therefore, against the nearly impossible task of covering developments occurring across the whole field, it seems reasonable for us to focus in this Perspective on one rapidly-developing direction within Plasmonics. Namely, we will discuss recent developments and insights in the study of the ultrafast dynamics of electrons in plasmonic meta- and nano-structures. This subject, which concerns the time evolution of excited charge carriers in plasmonic nanostructures under a pulsed excitation, is key to understand the physics of localized plasmons and how plasmonic nanostructures can potentially be utilized in practical devices.

Understanding the detailed time dynamics of the electron gas in a conducting crystal is a well-established problem within Condensed Matter Physics [7]. After being optically excited, the electron Fermi gas undergoes relaxation through different types of mechanisms, including electron-electron and electron-phonon scattering. Correspondingly, a practical theoretical approach can be constructed using the two separate temperatures of electrons and lattice [7,8]. Evaluating the evolution of these temperatures in time evidences an energy exchange between the Fermi electron gas and the gas of lattice phonons. This approach is now regarded as a two-temperature (2 T) model. An important, fundamental extension of the 2T model arises from the fact that not all excited electrons in a plasmonic nanostructure are thermalized and, therefore, one should further develop the formalism and introduce *an extended 2T model* [9–12]. In particular, such an extended 2T model is clearly formulated in Ref. [12], a publication that can be followed to use the model in practical calculations. The non-thermalized electrons are often regarded as hot electrons and their population becomes another, 3rd parameter. The resulting model is an extended 2T model [10,11,13]. This models allows for a quantitative description of the excited carriers' time dynamics in plasmonic nanocrystals [11,12], as well as for a description of photochemical processes [14]. Regarding the HEs, one should distinguish two kinds, thermalized and non-thermalized, a distinction that will be discussed below.

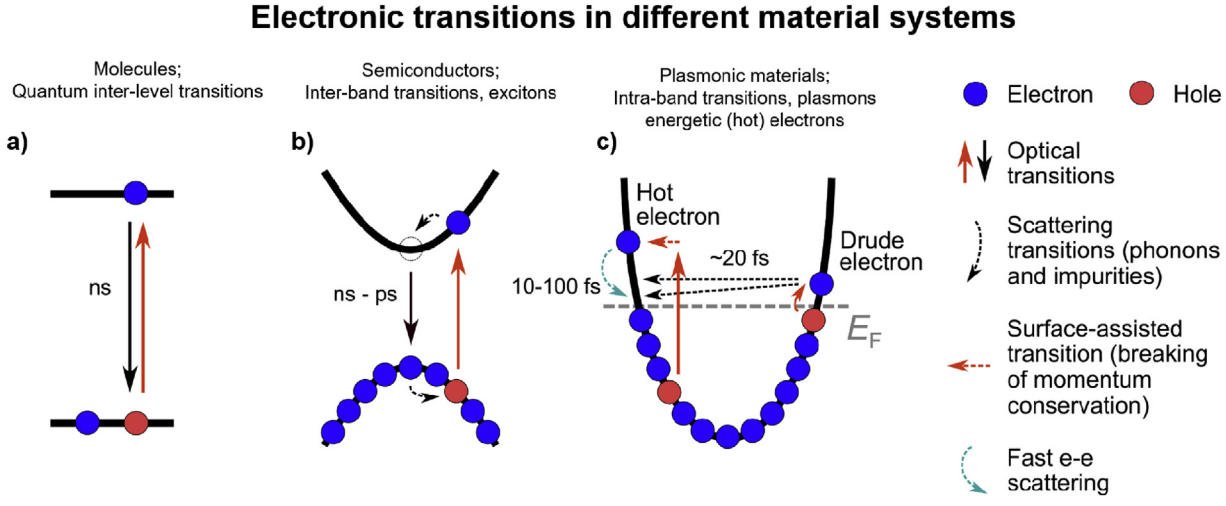


**Fig. 1.** Electronic transitions in different material systems. Energy spectra of quantum states (band diagrams) in different material systems and the main light-induced excitation channels available in them: **(a)** molecules, **(b)** semiconductors and **(c)** plasmonic crystals. Plasmonic crystals are conductive and can be, e.g. metals, degenerately doped semiconductors or conducting oxides. Also arising from the quantum structure of their states, these types of materials have fundamentally different relaxation mechanisms, depicted on the figure alongside their typical relaxation lifetimes.

When talking about experiential studies on the time-resolved dynamics of the electron gas in noble nanocrystals (NCs), one should mention the pioneering works by the French group [15–18] where the time dependent response was analyzed through both the 2T model and the local temperature-dependent dielectric function. Other early experiments on the dynamic properties of colloidal nanocrystals including electron-phonon and electron-electron relaxation processes can be found in Ref. [19]. Time-resolved experiments on single lithographical nanowires and the related application of the Boltzmann equation formalism were also presented in Ref. [12]. A pioneering study of the nonlinear properties of gold nanoparticles, which revealed the nonlinear pump-induced broadening of the plasmon resonance, was reported in Ref. [20], where this effect was interpreted in terms of the time-dependent electronic temperature. The investigation of single gold nanorods with variable sizes has also clarified the roles of interband damping and surface-scattering in plasmon relaxation [21].

Recent time-resolved experiments with short, 80 fs pump pulses in metamaterial absorbers with plasmonic hot spots reveal a very unusual dynamical feature, to which that we have referred as “anomalous ultrafast dynamics” [22]. The transient reflection observed in the pump-probe experiments exhibited an anomalously strong relaxation component in the fs-range. The pumping in this experiment was done in the spectral vicinity of the gap-plasmon resonance, which is located in the infrared interval. So far, plasmonic nanoparticles and nanorods have not exhibited such dynamical features and their kinetics have been mostly in the ps-range [15,19], which corresponds to relaxation through electron-phonon scattering. We attributed and explained the observed phenomenon of “anomalous ultrafast dynamics” as arising from a very efficient generation of hot electrons in the spatially extended plasmonic hot spots present in metamaterial absorbers with ultra-narrow spacer gaps between metallic antennas and film. Importantly, similar kinetics were later observed in metamaterials created using different systems as nanoantennas, namely colloidal silver nanocubes [23], confirming that the new effect of anomalous fs-relaxation is a general property of nanostructures with hot spots and infrared plasmons. The short lifetimes of excited carriers in these experiments, in the order of tens of fs, correspond to the temporal scale of electron-electron scattering. Here we should also note that another type of ultra-fast fs-relaxation dynamics appears in systems with semiconductor-metal interfaces where hot carriers are transferred across the boundary [24,25].

In addition to the recent time-resolved experiments, hot electron spectroscopy brings interesting possibilities in terms of spatial resolution. Hot-electron nanoscopy can be achieved with plasmonic tips in the tunneling regime [26,27]. Plasmon-driven excitation, including local hot-electron generation, underlies the key mechanisms in the processes of nano-localized surface chemistry and growth [28–31].

This Perspective is organized in the following way: In the first section we will describe the fundamental properties of plasmonic excitations in bulk and nanostructured metals, contrasting the classical and quantum perspectives. We will next present an overview of the experimental literature on time-resolved spectroscopy of plasmonic, non-interacting nanoparticles, as well as a theoretical model commonly employed to analyze those experiments in terms of the excited carrier populations in the nanoparticles, the so-called extended two temperature (2T) model. Such experiments will be contrasted with those in the following section, which are conducted instead on metamaterials with strong hot spots arising from their plasmonic gap modes. After that overview of key experimental works, we will present a more detailed discussion of the extended 2T model and our revision of it, to which we refer as quantum 2T model (Q2T), alongside a description of the relevant parameters required to characterize the non-equilibrium plasmonic system. This section also includes a selection of results from the latter model for a variety of representative geometries, and key experimental results supplying additional information on the energy-resolved non-equilibrium carrier populations. Next, we discuss the departure of excited carriers from the plasmonic system through tunneling or photoemission, presenting relevant experimental examples and the underlying physical phenomena. The final section describes in detail the last steps in the relaxation process of the excited plasmonic system, when the energy stored into the electronic degrees of freedom is transferred to the atomic lattice, exciting coherent oscillations of the nanoparticle, and how these are finally dampened in interacting with its environment. Lastly, we close this Perspective with an outlook of promising avenues for research, both in terms of improving our fundamental understanding of the time-dynamics of hot electrons and exploiting them in exciting technological applications.

## Dynamical properties of the Fermi gas in a nanocrystal: Fundamentals

### *Bulk plasmons, within the conventional approach*

We start with the case of charge oscillation in a 3D degenerate gas of electrons under weak optical excitation. Fig. 2a illustrates the plasmon oscillations of the Fermi sea of electrons, as excited by an external field. The oscillations occur both in real space and in momentum space (Fig. 2a). In the quasi-classical picture, the plasmon is well described by the Drude model, which is based on a hydrodynamic approach:

$$m^* \frac{d\bar{\mathbf{v}}}{dt} = \hbar \frac{d\bar{\mathbf{k}}}{dt} = e\mathbf{E} - m^* \gamma_{\mathrm{Drude}} \cdot \bar{\mathbf{v}} \tag{1}$$

where $\bar{\mathbf{v}} = \hbar\bar{\mathbf{k}}/m_0$ and $\mathbf{E}$ are the average velocity of electrons of the Fermi gas and the driving electric field, respectively, and $\bar{\mathbf{k}}$ is the average wave vector; $m^*$ and $\gamma_{\mathrm{Drude}} = 1/\tau_{\mathrm{Drude}}$ are the effective electron mass and the effective scattering constant of an electron in a crystal, respectively. For most metals, $m^*/m_0 \approx 1$, so in the numerical results presented herein we will assume this approximation for simplicity. Within the Boltzmann equation formalism, the time-dependent wave vector of electrons in the Drude equation (Eq. (1)) should be calculated as a value averaged over the electron distribution:

$$\bar{\mathbf{k}} = \frac{2}{(2\pi)^3 n_0} \int d^3k \cdot \boldsymbol{k} \cdot f(\boldsymbol{k}, t)$$

where $f(\mathbf{k}, t)$ is the electron distribution function and $n_0$ is the 3D electron density. Then, for the periodic driving field $\mathbf{E}(t) = \mathbf{E}_0 e^{-i\omega t}$, we obtain from (1):

$$\bar{\mathbf{v}}_\omega = \frac{e\mathbf{E}_0}{m^*(\gamma_{\mathrm{Drude}} - i\omega)} \tag{2}$$

The physical average velocity, which can be measured experimentally, should be now calculated as the real part of Eq. (2), $\bar{\mathbf{v}}(t) = \mathrm{Re}\left[\bar{\mathbf{v}}_\omega e^{-i\omega t}\right]$. Here we follow the conventional treatment, common in solid-state textbooks and used in a large number of experimental situations with bulk crystals and optoelectronic devices [1,32,33]. After solving the above equation, together with the Poisson equation, we can easily find the local conductivity and the dielectric function of a metal in the classical limit [32]:

$$\sigma^{\mathrm{D}} = \frac{e^2 n_0}{m_0(\gamma_{\mathrm{Drude}} - i\omega)}, \qquad \varepsilon^{\mathrm{D}}(\boldsymbol{\omega}) = \varepsilon_c - \frac{\omega_{\mathrm{p}}^2}{\omega(\omega + i\gamma_{\mathrm{Drude}})} \tag{3}$$

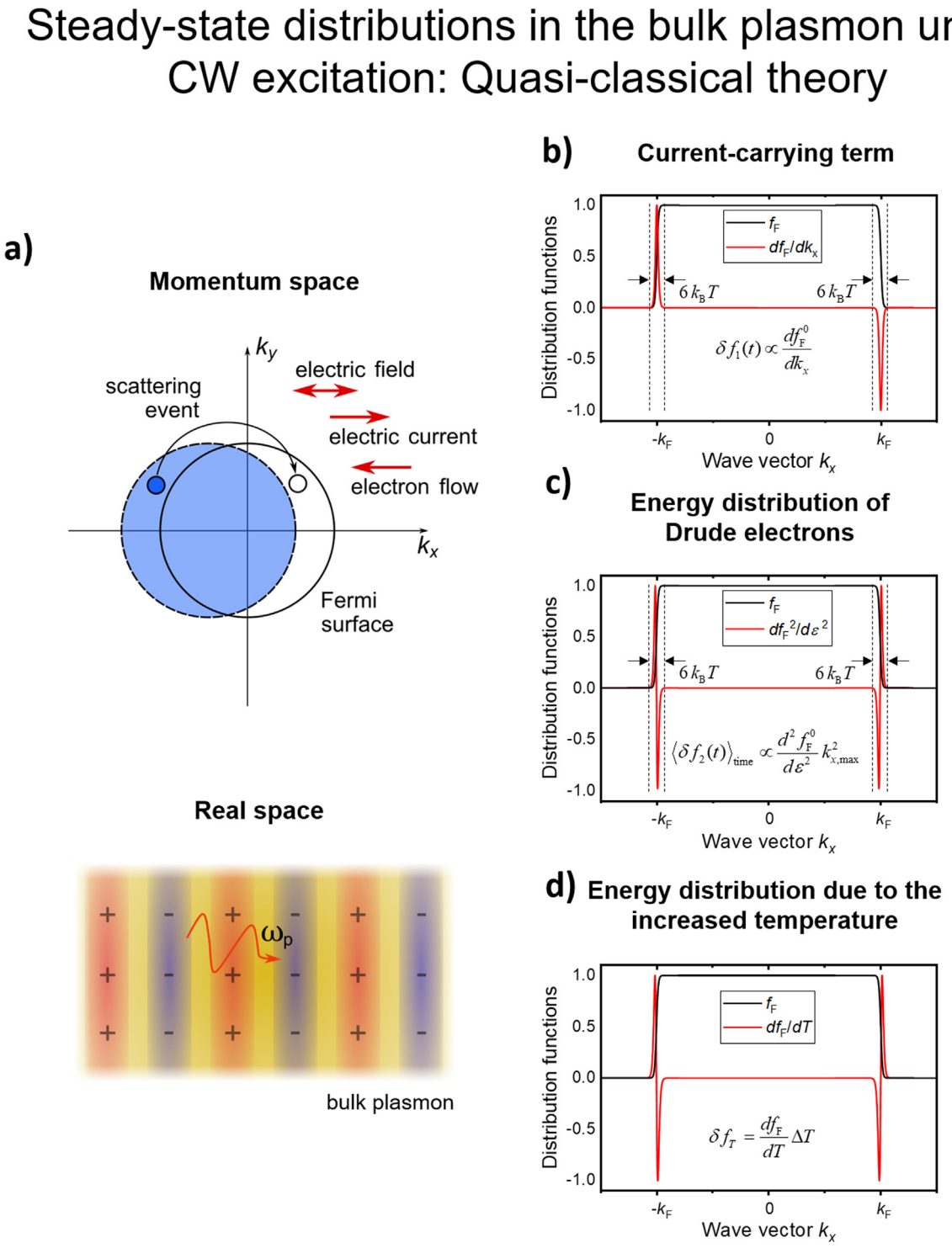


**Fig. 2.** Steady-state distributions in the bulk plasmon under CW excitation: Quasi-classical theory. **(a)** Oscillating Fermi sea within the hydrodynamic approach. The displacement of the Fermi sea from the center of coordinates in reciprocal space is described by the Drude model. Simultaneously, the plasmon wave creates charge oscillations in the real space [32]. **(b)** The linear, coherent part of the Boltzmann function that gives rise to the plasmonic current. The distribution is antisymmetric and therefore produces non-zero currents. **(c)** The second order term in the expansion in energy is symmetric and time-independent. It describes the generation of weakly-excited carriers, regarded here as "Drude" electrons, in the plasmonic wave. Such excited electrons have thermal energies. **(d)** The contribution of the first term of the expansion in temperature qualitatively resembles the function in panel (c), but it comes from an increase of the background temperature of the nanocrystal. In preparing panels (a) and (b) we followed the textbook by David Tanner [32]. We highly recommend this textbook for the reader.

where $\omega$ is the frequency of the external electric field and $\varepsilon_c$ is the background dielectric constant coming from the low-lying bands in a metal. The plasma frequency in (3) is given by

$$\omega_p = \sqrt{\frac{e^2 n_0}{\varepsilon_0 m^*}} \tag{4}$$

Then, according to the general theory of solids [3,33,34], the plasmon excitation in a boundless system is easy to find, calculated as the solution of $\varepsilon^D(\omega) = 0$. This yields $\omega = \pm\omega_p/\sqrt{\varepsilon_c} - i\gamma_{Drude}/2$ for $\omega_p \gg \gamma$. However, the physical picture of the plasmon oscillation is more apparent when we solve the Boltzmann equation

[32,34–36]. The distribution function, when derived from the Boltzmann equation, can be written in the hydrodynamic approach for small time-dependent driving fields as [37]:

$$f(\mathbf{k},t) = f_{\mathrm{F}}(\mathbf{k}-\bar{\mathbf{k}},T_{\mathrm{L}}), \quad \bar{\mathbf{k}}(t) = \frac{m^*}{\hbar}\bar{\mathbf{v}}(t) \tag{5}$$

where

$$f_{\mathrm{F}}(\varepsilon,T_{\mathrm{L}}) = \frac{1}{e^{\frac{\varepsilon-\mu}{k_{\mathrm{B}}T_{\mathrm{L}}}}+1}$$

is the Fermi function at temperature $T_{\mathrm{L}}$ and $\mu$ is the chemical potential of the system. The Fermi distribution without illumination is obviously

$$f_F^0(\varepsilon) = f_{\mathrm{F}}(\varepsilon,T_0)$$

where $T_0$ is the ambient temperature of the matrix and NC with no excitation. The lattice temperature of an optically-driven NC is above the one of the matrix at large distances from the NC, so that one could write $T_{\mathrm{L}} = T_0 + \Delta T_{\mathrm{L}}$. The lattice temperature increase $\Delta T_{\mathrm{L}}$ will depend on the size and environment of a NC [38]. Hereafter, we will assume that the electric field and currents in our system are in the x-direction (see Fig. 2a), i.e. $\bar{\mathbf{k}}(t)||\hat{\mathbf{x}}$. For weak optical fields, we can expand the hydrodynamic solution (Eq. (5)) in terms of the average wave vector $\bar{k}_x$ and obtain:

$$\begin{aligned} f(\mathbf{k},t) &\approx f_{\mathrm{F}}^0 + \frac{df_{\mathrm{F}}^0}{dk_x}\bar{k}_x + \frac{1}{2}\frac{d^2f_{\mathrm{F}}^0}{dk_x^2}\bar{k}_x^2 + \frac{df_{\mathrm{F}}^0}{dT}\Delta T \\ &= f_{\mathrm{F}}^0 + \delta f_1(\mathbf{k},t) + \delta f_2(\mathbf{k},t) + \delta f_T(\mathbf{k}) \\ \delta f_1(\mathbf{k},t) &= \frac{df_{\mathrm{F}}^0}{d\varepsilon}\cdot\frac{\hbar^2 k_x\bar{k}_x}{m^*} \\ \delta f_2(\mathbf{k},t) &\approx \frac{d^2f_{\mathrm{F}}^0}{d\varepsilon^2}\cdot\left(\frac{\hbar^2\bar{k}_x^2}{m^*}\right)\cdot\frac{\hbar^2k_x^2}{2m^*} \\ \delta f_T(\mathbf{k}) &= \frac{df_{\mathrm{F}}^0}{dT}\Delta T_{\mathrm{L}} \end{aligned} \tag{6}$$

The main message from Eq. (6) is in the forms of the terms $\delta f_1$ and $\delta f_2$, which allow us to better understand the underlying physics. The function $\delta f_1$ gives the electric current and has an antisymmetric structure in the k-space (Fig. 2b). In addition, the time average of this function is zero:

$$\delta f_1(t) \propto \frac{df_F^0}{d\varepsilon}\bar{k}_x(t), \quad \langle\delta f_1(t)\rangle_{\mathrm{time}} = 0 \tag{7}$$

This is because the average momentum in the plasmon wave is oscillating in time: $k_x(t) = k_{x,\max}\cos[\omega t+\varphi]$, where $k_{x,\max}$ is the amplitude of the oscillation. In contrast, the function $\delta f_2$ is symmetric in the k-space and its time average gives the steady-state population of excited carriers in the plasmonic wave:

$$\langle\delta f_2(t)\rangle_{time} \propto \frac{d^2f_F^0}{d\varepsilon^2}k_{x,\max}^2 \tag{8}$$

The last term in Eq. (6), $\delta f_T$, is time-independent under CW excitation. An important conclusion derived from Eqs. (6–8) is that the excited electrons responsible for the plasmonic wave are located near the Fermi energy. The characteristic width of the steady-state distribution of hot electrons in Fig. 2b–d is $6k_{\mathrm{B}}T$. The functions $\delta f_2$ and $\delta f_T$ look qualitatively similar, since they simply describe an increase of energy in the Fermi gas of electrons. This result was obtained assuming a boundless system and using the Drude model. In systems with boundaries and defects, one should expect some high-energy (hot) electrons and holes, and their generation should be derived with a quantum-mechanical formalism (Fig. 3b,c), as the quasi-classical approaches do not work for such carriers. We should also comment on the Drude relaxation constant. Using quantum kinetic theories, one can derive this constant rigorously [39]. The Drude rate is in fact the inverse of the transport relaxation time, which enters into the static electric conductivity and includes two contributions: $\gamma_{\mathrm{Drude}} = 1/\tau_{\mathrm{tr}} = \gamma_{\text{e-imp}} + \gamma_{\text{e-phon}}$, where $\gamma_{\text{e-imp}}$ and $\gamma_{\text{e-phon}}$ are the rates of quasi-elastic scattering by impurities and phonons, respectively. Fig. 4a shows such processes. The scattering of electrons by impurities is elastic, whereas the electron-phonon scattering is quasi-elastic since phonons carry small amounts of energy.

Regarding the fact that the plasmonic electrons under weak excitation should be found near the Fermi level, we highlight that this can be seen clearly from a solution of the Boltzmann transport equation. The plasmonic wave is built of a collection of coherently-excited electrons in the very vicinity of the Fermi level (Figs. 2a, 3b). The following books and papers are a very convenient source from which to read more on the electronic structure of the plasmon [32,34–36].

So far, we have discussed the quasi-classical picture. In the quantum formalism [34,39], we need to compute the quantum polarizability of the Fermi gas, from which one can derive the famous Lindhard expression for the dielectric function:

$$\varepsilon_{3D}(\omega,q) = \varepsilon_{\mathrm{metal},0} - \frac{e^2}{\varepsilon_0 q^2 V}\sum_k \frac{f_{\mathrm{F}}(\mathbf{k}) - f_{\mathrm{F}}(\mathbf{k}+\mathbf{q})}{\hbar\omega - \varepsilon_{\mathbf{k}+\mathbf{q}} + \varepsilon_{\mathbf{k}} + i\gamma_{\mathrm{rel}}} \tag{9}$$

where $\mathbf{q}$ is the wavevector of the external field applied to the Fermi gas, $V$ is the crystal's volume; $f_{\mathrm{F}}(\mathbf{k})$ and $\varepsilon_{\mathbf{k}}$ are the Fermi distribution function and the electron energy, respectively. In the long-wavelength limit $q << k_{\mathrm{F}}$ without collisions $\gamma_{\mathrm{rel}} \to 0$, Eq. (9) yields the classical limit: $\varepsilon_{3D}(\omega) = \varepsilon_{\mathrm{metal},0} - \omega_{\mathrm{p}}^2/\omega^2$. In the expression above, the key size parameter of the Fermi gas is its Fermi wave vector:

$$k_{\mathrm{F}} = m^* v_{\mathrm{F}}/\hbar$$

where the Fermi velocity is defined through the Fermi energy:

$$E_{\mathrm{F}} = \frac{m^* v_{\mathrm{F}}^2}{2} = \frac{\hbar^2\left(3\pi^2 n_0\right)^{2/3}}{2m^*}.$$

The characteristic length related to the electrons at the Fermi surface is called Fermi length:

$$\lambda_{\mathrm{F}} = \frac{2\pi}{k_{\mathrm{F}}} \sim n_0^{-1/3} = l_{\mathrm{e}}$$

where $l_{\mathrm{e}}$ is the average distance between electrons in the Fermi gas, which is rather short and in the order of the interatomic distance.

*Nanocrystals*

Under optical excitation, a metal nanocrystal exhibits plasmonic, collective charge oscillations with dynamic charges localized near its surfaces. (Fig. 3a). In fact, a NC acts as a small resonator. In the quantum-mechanical picture, the wave function of a plasmon is composed of a large number of single-particle electron-hole excitations in the electronic Fermi gas of the NC (Figs. 1c, 3 b). In the classical picture, the external field first excites electric currents in a NC and induces charges at the NC's surface. In the next step, this surface charge creates a restoring force that drives electric currents inside the NC, sustaining a plasmonic oscillation that repeats in time.

We now turn our attention back to the illustrations of the physical processes happening in an optically-excited Fermi gas in a plasmonic NC (Figs. 1c,3), where the boundaries play important role. In fact, due to the boundaries, we can find some number of non-thermalized hot electrons in a plasmonic wave. The classical picture of a plasmon wave assumes the excitation of electron-hole pairs with small energies, and this picture is well described by the hydrodynamical approach known as the Drude model (Eqs. (1)-(3)).

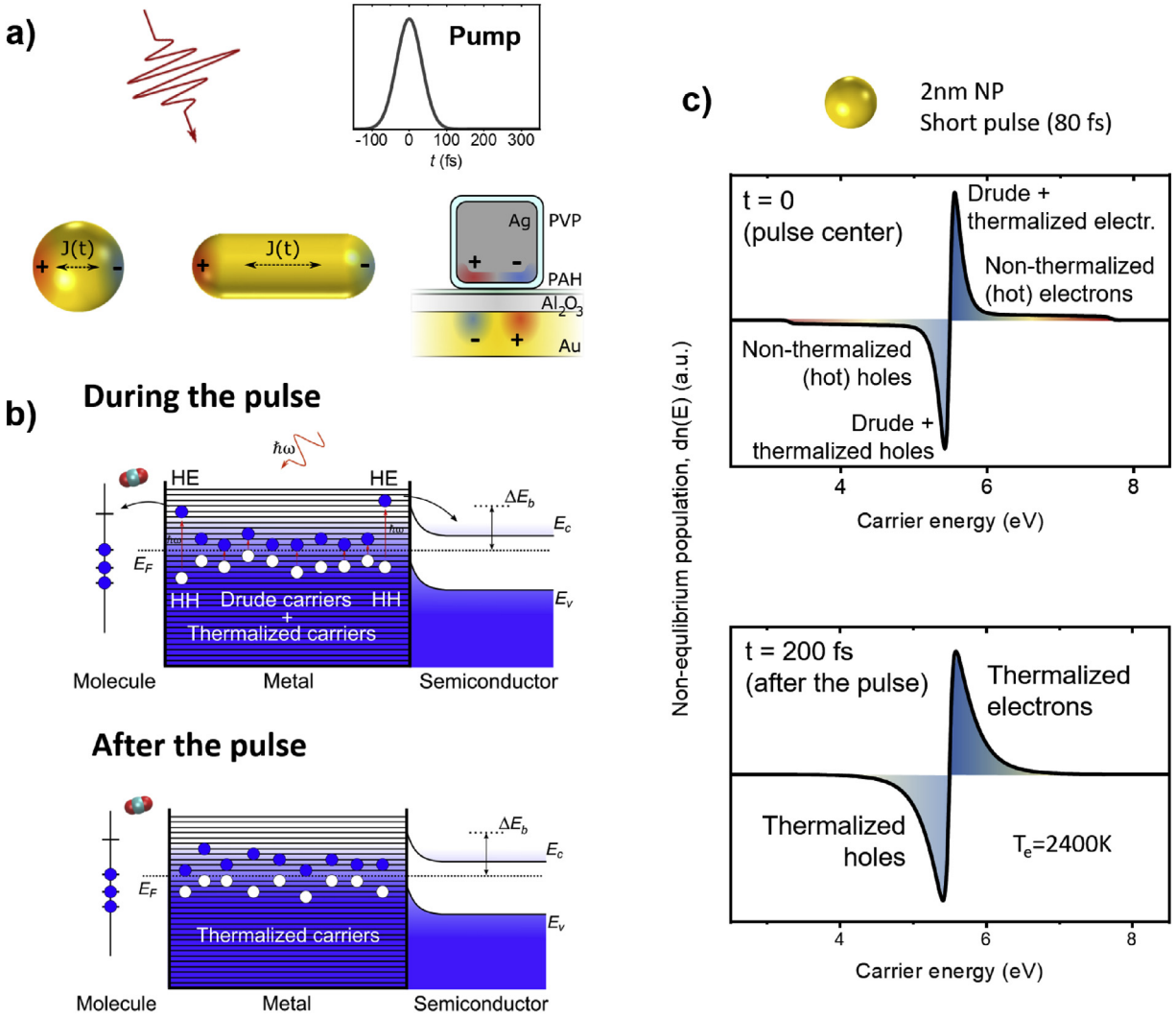


**Fig. 3.** Charge carriers in a localized plasmonic excitation. **(a)** Schematic depiction of typical localized plasmonic modes in nanostructures with different shapes, when excited by a short optical pulse, or pump, represented above. **(b)** Diagrams showing the picture of the electronic states of a metal NC in interaction with adjacent semiconductor and molecule, during (top panel) and after (bottom panel) the pulse excitation. At first there is a mixture of Drude (in the bulk) and hot (at the surfaces) carriers, while after some time the hot carriers have shared their energy among the rest of the carriers, creating a picture with a higher, homogeneous effective electron gas temperature. Drude carriers arise from the electric current associated with a localized plasmonic wave. After the pulse, the plasmonic oscillation decays rapidly, leaving thermalized carriers which can have a high electronic temperature. The top diagram also illustrates how non-thermalized (hot) electrons with energy above certain threshold can be injected into the neighboring systems. Such non-thermalized (hot) electrons with high energies appear near the surfaces because of the non-conservation of electronic linear momentum. **(c)** Snapshots of the electronic distributions in a very small spherical Au NC, calculated using the quantum 2T model, showing populations for Drude and HEs. Details on this calculation are provided in the text. Here we see that, even in a very small NC, the number of high-energy (hot) electrons is small in comparison with the number of carriers with small excitation energies, labeled here as Drude and thermalized electrons.

This picture corresponds to electronic excitations near the Fermi level with small linear momenta (Fig. 1c). However, since the electron gas inside a NC is confined by its boundaries, the linear moment of electron is not conserved near the interfaces, where the translational symmetry of the system is broken. As a result, the excitation of non-thermalized hot electrons (HEs) and hot holes (HHs) with high energies becomes possible (Figs. 3b and 5). The energies of such energetic carriers are as high as the photon energy, $\hbar\omega$. In Fig. 3b, we show the picture of electronic excitation in a localized plasmonic wave: the carriers excited in the bulk of a NC correspond to those described by the classical Drude model (see above) and have small energies, whereas the spatial regions near the boundaries see the promotion of a number of high-energy electrons and holes, or HEs and HHs. Importantly, these energetic carriers can be extracted from a metal NC and drive secondary processes outside a NC [40]. In Fig. 3c, we show a typical nonequilibrium electron distribution of excited electrons in an NC under a pulse excitation. The nonequilibrium population is defined as

$$\delta n(\varepsilon) = \frac{dN_{\text{nonequilibrium}}}{d\varepsilon} = n(\varepsilon) - n_F^0(\varepsilon) \tag{10}$$

where $n(\varepsilon) = dN/d\varepsilon$ is the distribution of electrons over energy in a NC, $N$ is the number of electrons in a NC and $n_F^0(\varepsilon) = f_F^0(\varepsilon) \cdot DOS(\varepsilon)$ is the Fermi equilibrium distribution; $f_F^0(\varepsilon)$ and $DOS_e$ are the Fermi function at the ambient temperature $T_0$ and the density of states, respectively. In Fig. 3c we show the energy distributions at two times: during the pulse ($t = 0$) and after the pulse ($t = 200$ fs). During optical illumination, i.e. at $t = 0$, we observe in Fig. 3c that the Fermi sea is out of equilibrium: the function $\delta n(\varepsilon)$ is positive above the Fermi level ($\varepsilon > E_F$) and negative for the energies below the Fermi surface ($\varepsilon < E_F$). During the pulse, we observe populations of HEs and HHs with high excitation energies in the energy interval $E_F + \hbar\omega > \varepsilon > E_F - \hbar\omega$. The number of such carriers is relatively small since they are created preferentially near the surfaces [41], as electron scattering at the surfaces breaks the conservation of the electronic linear momentum, thus allowing transitions with large

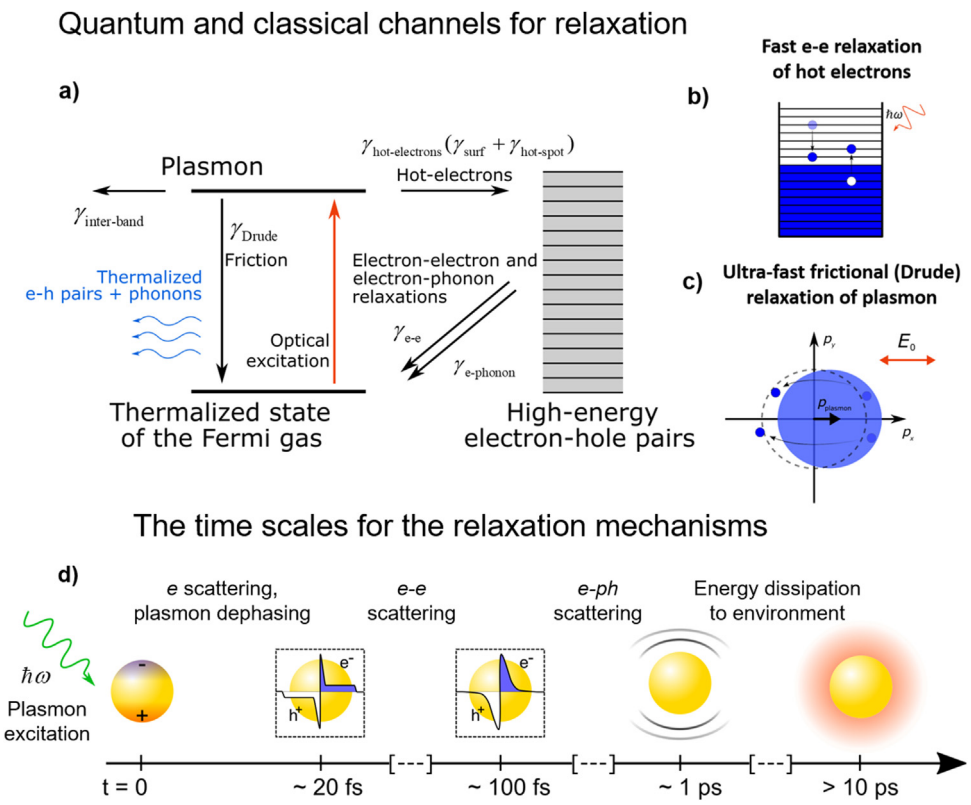


**Fig. 4.** Collective and single particle relaxation processes and timescales. **(a)** Diagram of the processes of plasmon decay. The text explains in detail the relaxation channels shown in this panel [41]. **(b, c)** Illustrations for two important mechanisms of relaxation: (b) fast energy relaxation of hot electrons due to e–e scattering and (c) ultrafast momentum relaxation of plasmon due to the frictional Drude force [41]. Panel **(d)** depicts the sequence of events and approximate timescales involved in the excitation and decay of plasmon and charge carriers following the absorption of photons by a metal nanoparticle [48]. Panels (a)-(c) were reproduced with permission from [41]. Copyright 2017 American Chemical Society.

$\Delta k$ (Fig. 5a). This stands in contrast with the excitation of Drude electrons, which is a bulk-like process (Fig. 5a,b). Importantly, the generation of these high-energy carriers is not only facilitated by electron-surface scattering (Fig. 5c), but also by the intense field gradients characteristic of plasmonic hot spots (Fig. 5d,e). However, such carriers have very short lifetimes due to the frequent electron-electron collisions in the Fermi gas (Fig. 4). Simultaneously, we observe large numbers of excited electrons near the Fermi level, for which we use the label "Drude" electrons; these excited electrons form electric currents in the classical plasmonic wave (Fig. 5a,b). The classical (Drude) and quantum (hot) excited electrons in the plasmonic wave are also associated with two different mechanism of decay for the plasmon (Fig. 4). Let us now look at the electronic state of a NC after the pulse, at $t = 200$ fs. In this case, the coherent plasmonic oscillation has already decayed, but the Fermi gas still holds the absorbed optical energy. We do not see any more HEs and HHs, but the system has a distribution of thermalized electrons (with the thermalization process occurring owing to rapid electron-electron collisions) to a high nonequilibrium electronic temperature. The following step of the electronic relaxation will see the thermalization between the warm (thermalized) electrons and the lattice phonons. At this step, the extra electronic energy will be depleted while increasing the lattice temperature, which happens within a few picoseconds.

Fig. 4 summarizes the relaxation mechanisms for a plasmon and for excited electrons [41,42]. The rate of decay of a plasmon (which is the inverse of its lifetime) has the following contributions (Figs. Fig. 4a, 5c,d) [42]:

$$\gamma_{\text{plasmon}} = 1/\tau_{\text{plasmon}} = \gamma_{\text{bulk}} + \gamma_{\text{rad}} + \gamma_{\text{surf}} + \gamma_{\text{hot-spot}} \quad (11)$$

where $\gamma_{\text{rad}}$ corresponds to the radiative decay rate, covering the process by which the dipolar moment of the plasmon oscillations triggers the reemission of a photon to the far-field, and $\gamma_{\text{bulk}}$ is the decay rate of a plasmon in bulk, which can be further subdivided in two components,

$$\gamma_{\text{bulk}} = \gamma_{\text{Drude}} + \gamma_{\text{inter-band}}$$

The above contributions represent two mechanisms of electron scattering; $\gamma_{\text{Drude}}$ is the rate of relaxation of electron momentum in a plasmonic wave and this rate enters the hydrodynamic Drude model (Eqs. (1), (2)); the related term $-\gamma_{\text{Drude}}\mathbf{v}$ in the hydrodynamic equation (Eq. (1)) can be interpreted as a frictional force and originates from electron scattering by phonons and defects in a crystal. The rate $\gamma_{\text{inter-band}}$ comes from optical inter-band transitions, which are also available in metals for photon energies above a certain energy that depends on the material; they become relevant as a plasmon decay mechanism when the plasmon frequency is in the blue or UV spectral intervals. Finally, the most interesting term in Eq. (11) is the surface scattering and hot spot contributions, $\gamma_{\text{surf}}$ and $\gamma_{\text{hot-spot}}$, respectively [41]. The first term is often called the Kreibig's term [43–45] (Fig. 6), and depends strongly on the NC's size, as

$$\gamma_{\text{surf}} = A \cdot \frac{v_{\text{F}}}{a_0} \quad (12)$$

where $a_0$ is the NC diameter, $v_F$ is the Fermi velocity of the material and $A$ is a numerical constant [43,46,47]. Several experiments with NCs of variable sizes confirmed the characteristic size dependence of the surface scattering rate of the plasmon [46–48], and Fig. 6a shows a selected result from the relevant literature. Mathematically, Kreibig's term, in Eq. (12), is the classical frequency

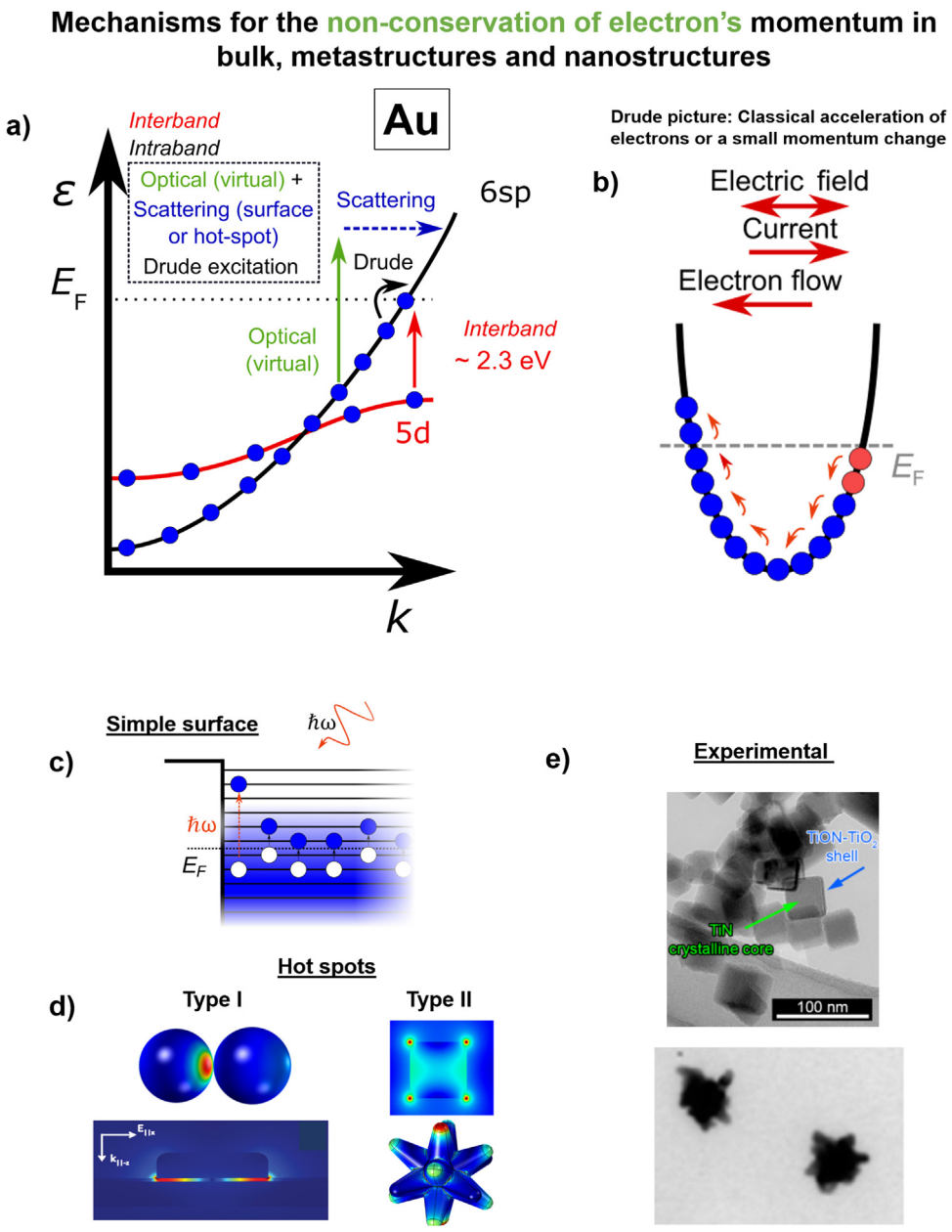


**Fig. 5.** Mechanism for the non-conservation of electron's momentum in bulk, metastructures and nanostructures. **(a)** Schematic diagram of the band structure of gold, noting the relevant transitions that the electrons can undergo under illumination. These are separated as inter- and intraband transitions, and we further differentiate two possible categories of the latter: Drude excitations and transitions involving a scattering event that causes a large change of electron momentum. **(b)** Diagram showing the Drude picture, or the classical displacement of the electrons in a collective response to external electromagnetic radiation. The total photon energy is distributed across all carriers. On the other hand, the non-conservation of the electron momentum allows individual carriers to become excited to energies up to the total photon energy, and these can occur through their scattering at the metal surface **(c)** or through the strong field gradients in hot spots **(d)**. Panel (d) illustrates two distinct types of hot spots, those created by gap modes [22,58], and those arising from sharp geometrical features in NCs [41,59]. **(e)** TEM images of two different types of systems exploiting plasmonic hot spots of the second type, namely TiN nanocubes and Au nanostars [60,61]. Reproduced and adapted with permission from (d) [22,41,58,59] Copyright 2015 Nature Springer, 2017 American Chemical Society, 2017 Wiley, (e) [60,61] Copyright 2016 American Chemical Society, 2017 Wiley.

of collisions of a ballistic electron with the NC boundary. However, the physical origin of this term lies in quantum mechanics. This term comes from the scattering of electrons near the surfaces, where the electron momentum is not conserved. In this way, a plasmonic excitation can be converted to high-energy electron-hole pairs (Fig. 6b). This process of generation of HEs and HHs occurs near the walls of a NC, where the dynamic charge of a localized plasmon wave shows the so-called Friedel oscillations (Fig. 6c), which are a feature of the dynamic screening of a Fermi gas. The structure of the electronic states near the surface and, in particular, the spill-out of their wave functions are important for a numerical description of the HE generation and the surface-induced damping of the plasmons [47,49]. In plasmonic photochemistry, the Kreibeg's mechanism of plasmon damping is often compared with the effect of the so-called chemical interface damping [50].

Recently, theoretical studies [41,58] pointed out the existence of a novel mechanism of generation of HEs related to plasmonic hot spots. Like in the surface scattering mechanism, an efficient generation occurs due to the non-conservation of the linear momentum of an electron. This non-conservation process takes place in small volumes of a NC with strong field gradients, which we often regard

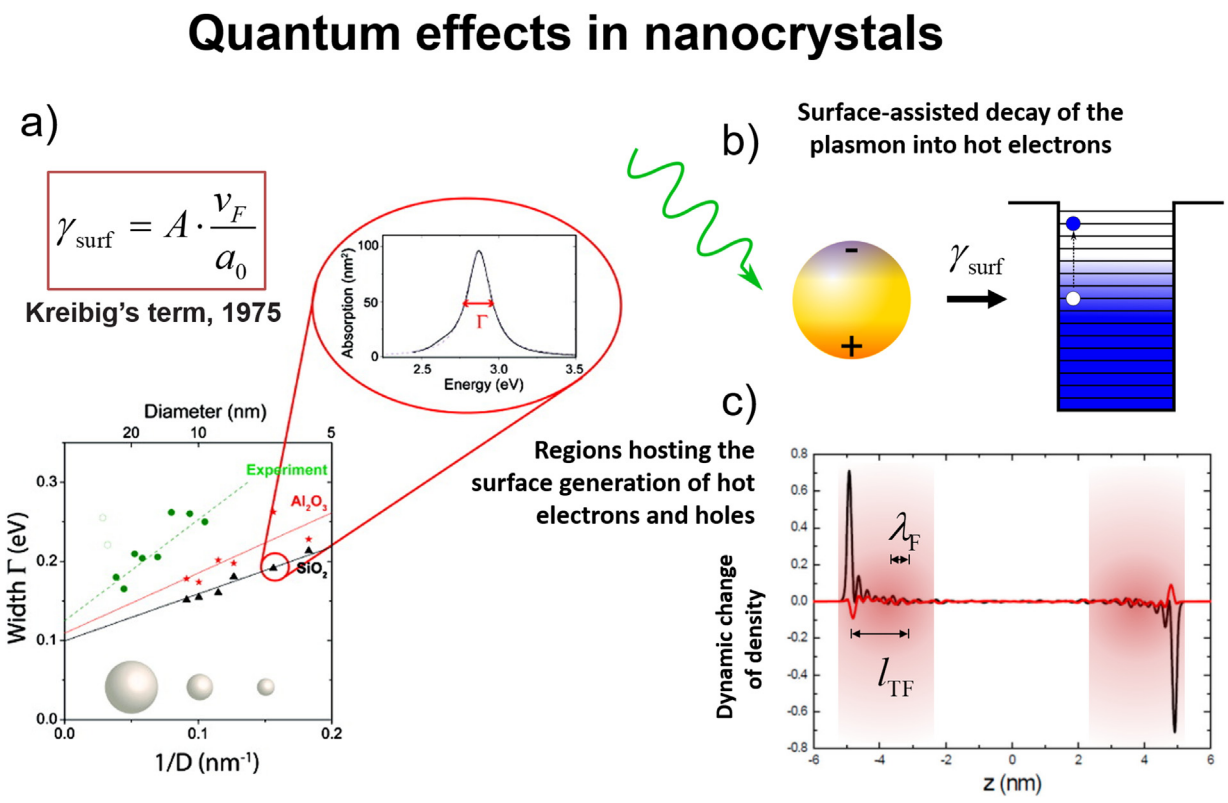


**Fig. 6.** Quantum effects in nanocrystals: Surface effects. Information and diagrams illustrating Kreibig's physics [43,44]. **(a)** The famous Kreibig's equation modelling the quantum channel of plasmonic decay owing to the scattering of electrons at the interface [47]. **(b)** The decay process in the quantum picture, with the energy of the plasmon is transferred to an electron-hole pair interacting with the NC's surface. **(c)** Friedel oscillations of the dynamically screened charges at the interfaces, differentiating the real process from an ideal classical accumulation of charge at the surfaces [49]. Panel (a) was reproduced with permission from [47]. Copyright 2011 ACS.

as hot spots (Fig. 5c–e). Such special volumes, hot spots, typically appear at the apexes of NCs with complex shapes (Fig. 5e). We note that hot spots can also appear near flat surfaces, and one example is the case of planar metamaterial absorbers with narrow gaps [22,23]. Whereas SERS and related plasmon-enabled molecular spectroscopys techniques utilize hot spots outside a NC, the hot spots that are relevant for the hot electron effect are located inside the metal.

The relaxation processes in an excited Fermi gas also include decay mechanisms for single electrons. Fig. 4 provides a summary of such mechanisms. Single excited electrons can lose their energy via fast electron-electron scattering (e-e scattering) or via emission of non-equilibrium phonons (Fig. 4a). Fig. 4d illustrates the different timescales involved in the general relaxation process. The fastest relaxation mechanism is the frictional one and its decay rate enters the Drude dielectric function. The lifetimes of HEs are also short, ~100 fs or shorter, and arising from e-e scattering. On the other hand, electron-phonon scattering timescales are typically in the ps range and heat diffusion is relevant after 10 ps and longer (Fig. 4d). These timescales and their related relaxation mechanisms are needed to interpret experiments with plasmonic dynamics in NCs.

To conclude this section, we point out to a few useful review papers which describe the subject of plasmonic and electronic decay mechanisms. An excellent review on time dynamics and related experiments, with emphasis on single-particle spectroscopy, can be found in Ref. [48]. The physics of HEs in nanostructures were reviewed in Refs. [41,51,52]. Time-resolved and single-particle studies of nanocrystals with simple shapes were well described in Refs. [15,42,53,54]. Some other recent reviews on the applications of HEs for photochemistry can be found in Refs. [40,55–57].

### Time-resolved experiments with simple particle shapes

When a NC has a simple shape, such as a rod or a sphere, the relaxation dynamics involved, measured via time-resolved absorption or scattering of a secondary beam, occur fundamentally in the picosecond time range (Fig. 7). They are governed by electron-phonon relaxation and lead to the equilibration of electronic and lattice energy reservoirs, with the corresponding balancing of their effective temperatures. However, one can recognize contributions from the ultra-fast femtosecond dynamics associated with the e-e relaxation of HEs [12]. This is accomplished by using an extended 2T model, based on three parameters, to analyze the complex dynamics of hot and warm electrons [12].

There is a growing literature on time-resolved spectroscopy of plasmonic films and nanocrystals with simple shapes [15,19,42,48,54,62]. In such experiments, a short femtosecond pulse is used to excite a system and another short pulse sent with a known time delay is then utilized to read out the state of the electronic gas in the NC (Fig. 7a). Here we will give a few snapshots directly taken from this body of research, starting from the transient transmission signals observed in an ensemble measurement of spherical Au NCs (upper panel in Fig. 7a) [20]. During the pump pulse (200 fs long), one can see the appearance of a characteristic transient signal (one positive peak and two negative features to its sides) that should be interpreted as an optically-induced broadening (damping) of the plasmon peak (upper panel in Fig. 7a). The physical reason for the increased damping of the plasmon is the dramatically increased temperature of the electron gas, rising up to 4000 K for the pulse intensity used in that study (lower panel in Fig. 7a). At such temperature, a few mechanisms can contribute to the nonlinear damping, such as inter-band relaxation, electron-phonon (e-ph) scattering and e-e scattering.

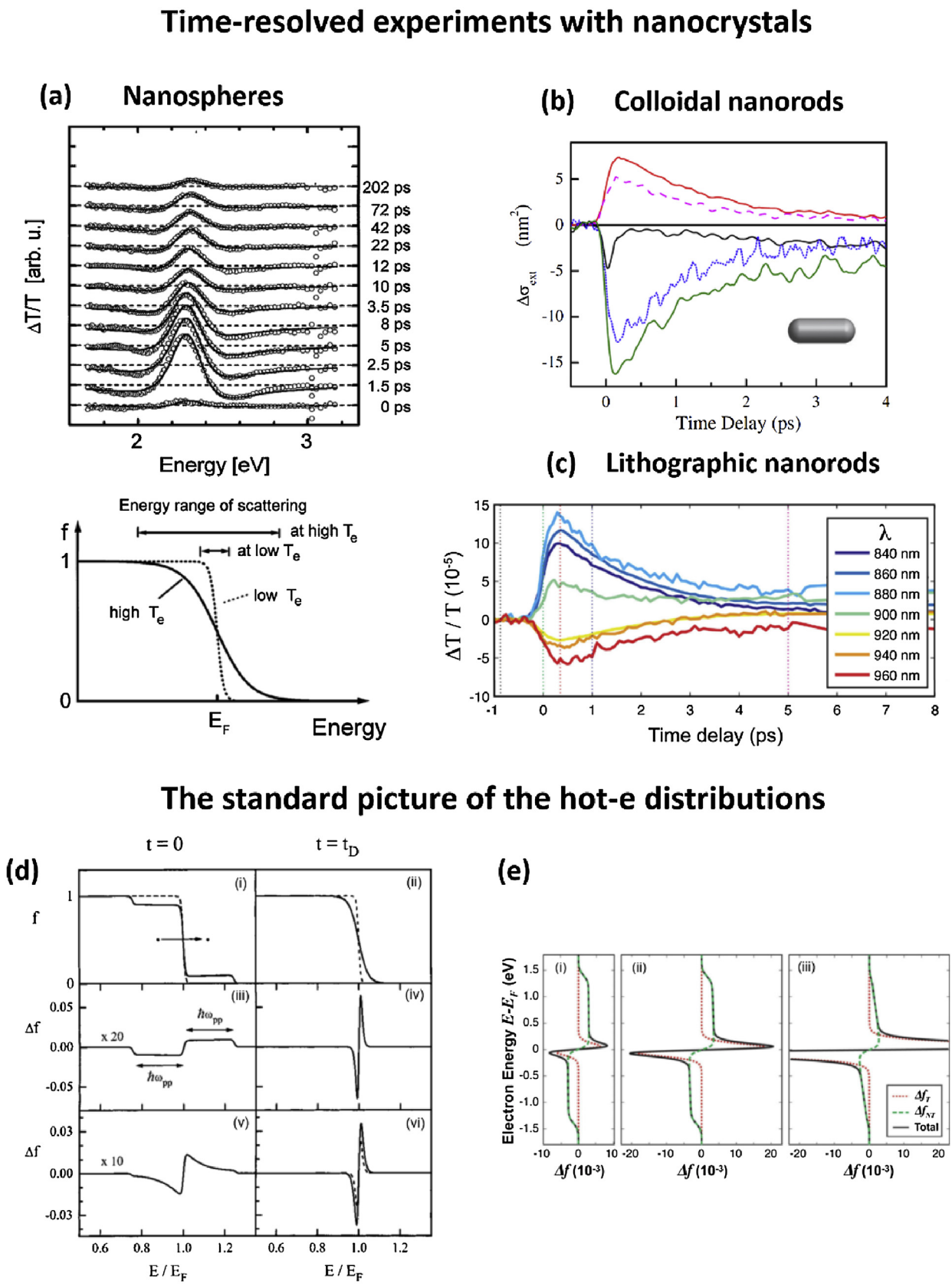


**Fig. 7.** Selected time-resolved pump-probe experiments with nanocrystals and classical extended 2T model of carrier excitation. Panels (a–c) are taken from selected experimental studies, while panels (d,e) illustrate the theoretical picture of the classical extended 2T model. **(a)** Differential transmission $\Delta T/T$ versus probe-photon energy at different time delays for gold colloids embedded in a sol-gel matrix (top panel). The bottom panel shows schematic Fermi distribution functions at low (dashed line) and high (solid line) electron temperatures, representing the general process by which the pump changes the electronic energy distribution in the metal [20]; **(b)** Time-dependent change in extinction cross section measured for gold nanorods (inset, 43 nm × 12 nm) at different probe wavelengths $\lambda_{pr}$ around its resonance (from top to bottom, $\lambda_{pr} - \lambda_R \approx 30, 40, 0, -30$, and -20 nm). The response when probing at the plasmon resonance shows a distinct, ultrafast time response and a posterior slow signal increase [18];

Two examples of transient dynamics of the optical response of single nanorods are shown in Fig. 7b,c [12,18]. The main relaxation times of these dynamic data are in the picosecond range and are attributed to e-ph relaxation. The signs of the signals were described explained using the local dielectric model. A local dielectric function of gold includes the contributions of the frictional intra-band response (Drude model) and the inter-band processes. Both parts of the local dielectric constant depend on the electronic and phononic temperatures. In the case of Ref. [12] (Fig. 7c), the dynamics were analyzed using an extended 2T model (sometimes referred in the literature as a 3T model), which incorporates ultra-fast e-e relaxation. Such relaxation is not seen directly by eye in the traces, but a careful numerical analysis can reveal it. In the following section, we will show a very different case, in which an ultra-fast femtosecond component is clearly visible and completely dominates the dynamics at short times after the pump pulse excites the particles.

The panels of Fig. 7d,e show typical electronic distributions at different times, which weremodeled in the context of electronic temporal dynamics in an ultra-fast time-resolved experiment [11,63]. In Fig. 7d, one can see the electron distributions at the center of a pulse ($t = 0$) and at the time of thermalization ($t = t_D$). At $t = 0$, the nonequilibrium part of the distribution is postulated as having a flat shape (2nd row). In the 3rd row of Fig. 7d, one can see the nonequilibrium population $\Delta f$, which is based on the empirical formula involving the electronic density of states. Both nonequilibrium populations $\Delta f$ assume that the electronic momentum is not conserved under optical excitation. This is, of course, not true and the momentum conservation plays a major role in constraining the electronic dynamics. This issue will be addressed in the following sections. It will be shown that the quantum-mechanical calculation should give very different pictures for the states of the electronic system at small times (i.e. during and just after a pump pulse). The calculated data in Fig. 7e were obtained using the Boltzmann equation and utilizing the fact that the total energy in the electron system is conserved in the e-e relaxation. Again, we see here that the nonequilibrium function $\Delta f$ has flat regions for HEs and HHs at $t = 0$, which later decrease in magnitude while we observe a strong growth of the number of low-energy thermalized electrons. The number of low-energy electrons is so large because the e-e scattering conserves the total energy in the electron gas. The modelling shown in Fig. 7e is based on the extended 2T model, in which the initial energy is converted only into the HEs. In our quantum 2T model [41], we show that this is not so. The reason lies in the conservation of linear momentum in the electronic excitations and in the creation of large numbers of excited carriers with small energies. We regard such carriers as Drude electrons [41].

## Anomalous dynamics in metastructures: hot spots with gap plasmons in the infrared

As mentioned above, this section will provide interesting examples of structures where the unusual ultra-fast dynamics dominate the temporal responses at short times after excitation. A detailed understanding of the dynamics of hot electrons is necessary for, ultimately, finding pathways to use them in applications that include different approaches for solar energy conversion, including photocatalytic processes such as water splitting [51,55,64–69]. However, performing dynamical studies of hot plasmonic electrons is challenging, primarily because (a) the low generation efficiency of non-thermalized hot electrons in most plasmonic nanostructures makes them difficult to detect and (b) the very fast decay dynamics of non-thermalized carriers limits the techniques that can be used to detect them. Addressing this issue, we have recently reported on the ultrafast pump-probe spectroscopy of gap-mode plasmonic metamaterials which are configured similarly to super absorbing metamaterials (schematic in Fig. 8 a), and that show an anomalously high production of non-thermalized carriers [22,23].

The studied metamaterials supporting plasmonic gap modes generally consist of a gold film approximately 50 nm thick, upon which the atomic layer deposition (ALD) technique is used to grow a 4–25 nm thick spacer layer. This layer is usually a large band gap material such as alumina ($Al_2O_3$), but materials with smaller gaps, e.g. $TiO_2$, have also been explored [22]. The ALD process can create uniform spacer thicknesses with sub-nanometer precision. Finally, a gold or silver nanoparticle, either fabricated through lithography or deposited after being synthesized colloidally, is placed on the spacer layer. An example of the deposition of silver colloidal cubes, with an edge dimension of 150 nm, on top of an $Al_2O_3$ film is shown in Fig. 8b. The deposition process is such that the colloidal cubes are sparsely dispersed on the substrate, avoiding interparticle coupling that would lead to strongly heterogeneous behavior [23]. This approach also allows a large area deposition, important for enabling a sufficient signal to noise ratio in ultrafast transient absorption spectroscopy, with areas larger than a square centimeter as shown in Fig. 8b.

The ultrafast transient absorption spectra are obtained in reflection mode in near-normal incidence. Due to the absence of transmitted light through the metamaterial, absorption can be directly obtained from measured reflection via the relation Absorption = 1 – Transmission – Reflection. The transient absorption spectrometer has been described elsewhere, but we can briefly comment some of the relevant details of the setup. The pump wavelength is selected with an optical parametric amplifier coupled to an amplified Ti:sapphire laser [22,23]. A small amount (5%) of the Ti:sapphire output is used to create a continuum probe by focusing into a sapphire or $CaF_2$ (which has extended UV generation) window. Silicon (visible) and InGaAs (near-IR) detectors are used to acquire each spectrum as a function of probe delay (using an optical delay line). The stitched 3D spectrum shown in Fig. 8c is the final result, with transient absorption plotted as a function of optical delay vs. wavelength. Fig. 8d shows one "cut" at a delay of 35 fs when the sample is optically excited at the gap plasmon resonance at 1100 nm, along with the ground state absorption spectrum of the metamaterial. An ultrafast broadband optical response is produced as a result of the multiple resonances present in the gap plasmon metamaterial. The ultrafast response is generally spectrally narrower than the ground state response due to a degree of

**(c)** A similar observation can be made on the experimental $\Delta T/T$ time traces for a gold nanoantenna (170 nm × 50 nm) probed at its resonance (900 nm, green curve), after being pumped at 780 nm [12]; **(d)** Theoretical data from the extended 2T model for Ag presented in Ref. [63]. Panels in the left column (i, iii, v) depict the electron energy distribution during the pulse, while panels in the right column (ii, iv, vi) depict it after a time delay $t_D$ sufficient for the thermalization of the hot electrons. Panels in the first row (i, ii) show the equilibrium ($f_0$, dashed line) and initial athermal ($f$, full line) electron occupation number assuming instantaneous intraband excitation by a pump pulse of frequency $\omega_{pp}$. The remaining four panels show the corresponding change in the population $\Delta f = f - f_0$ around $E_F$ for the athermal and thermal situations, with (iii, iv) representing the same picture than panels (i-ii), and (v, vi) showing actual results from the model at $t_D = 0$ fs and, in panel (vi), $t_D = 400$ fs and 1 ps (full and dashed line, respectively) [63]; **(e)** Theoretical reconstruction of the variation of thermal (T) and non-thermal (NT) electron energy distribution in excited thin gold films at different time delays after being optically pumped. In this picture, the pump initially excites a population of hot electrons that, in a second step, distribute their energy through electron scattering and populate a non-equilibrium thermalized electron energy distribution [11]. Reproduced with permission from (a) [20] Copyright 1997 American Physical Society, (b) [18] Copyright 2011 American Physical Society, (c) [12] Copyright 2015 American Chemical Society, (d) [63] Copyright 2001 American Chemical Society, (e) [11] Copyright 2012 American Physical Society.

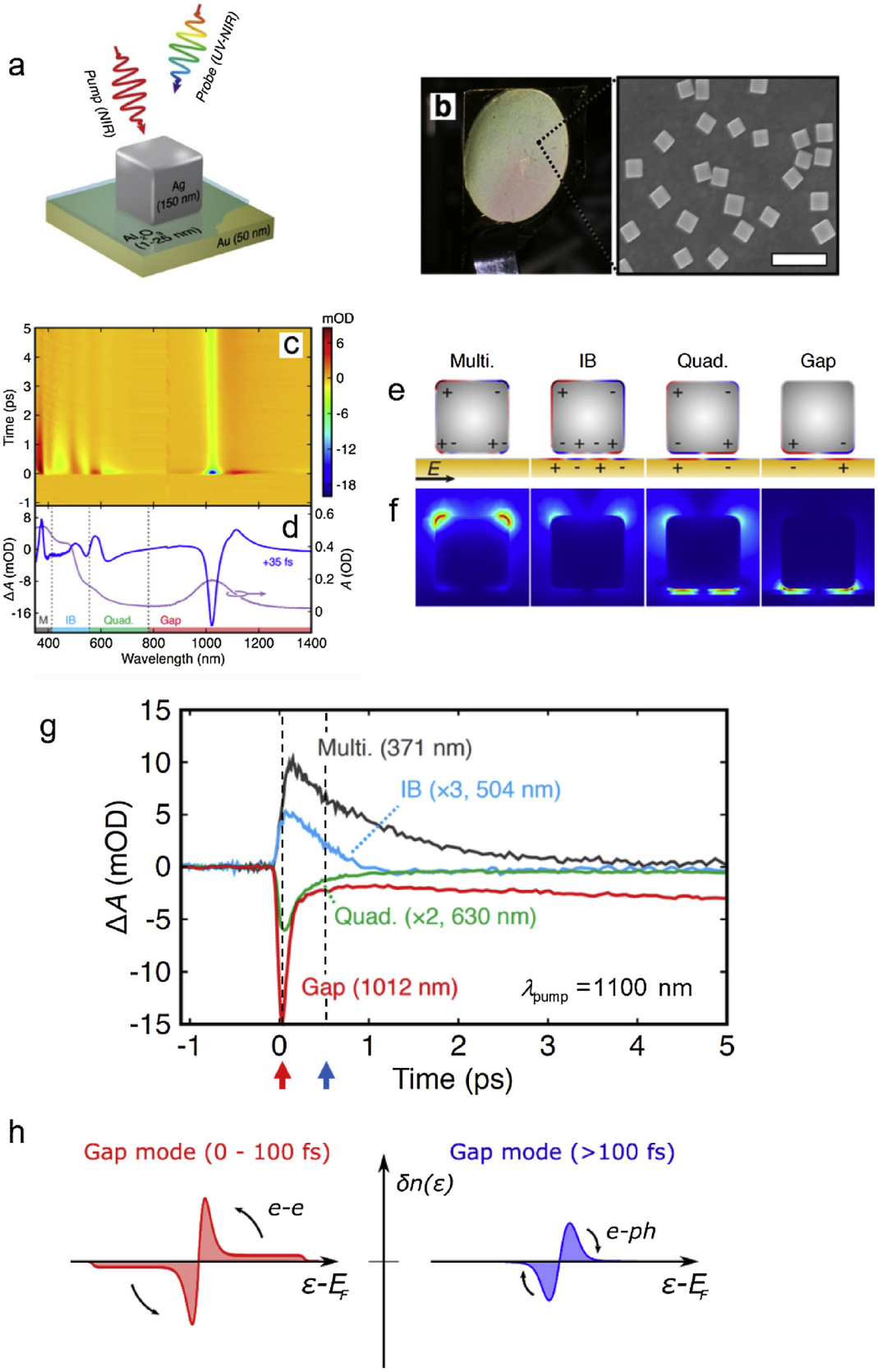


**Fig. 8.** Pump-probe time-resolved spectroscopy on metamaterials with plasmonic gap modes. **(a)** A schematic of the gap-plasmon structure and pump-probe experiment. A Ag nanocube is separated from a thin gold film by a thin spacer layer. **(b)** A photograph of an 1 cm diameter deposition of Ag nanocubes to create the gap-plasmon metamaterial and a scanning electron micrograph image of the distributed Ag nanocubes (scale bar = 500 nm). **(c)** The 3D transient absorption spectra of the metamaterial excited at the gap plasmon resonance of 1100 nm. **(d)** A single transient spectrum for a delay of 35 fs is shown along with the ground state absorption spectrum of the metamaterial. **(e)** An illustration of the different modes and resonances of the gap plasmon metamaterial. **(f)** Modeled electromagnetic field distributions for each mode and resonance feature. **(g)** Ultrafast transient absorption decay kinetics at each resonance feature. Strong evidence for the presence of non-thermalized electrons is shown, particularly via the ultrafast

heterogeneity of the sample that results in a subset of nanocubes being excited at a given excitation wavelength.

The use of silver nanocubes with a gold film in a gap mode geometry produces several resonance features which are illustrated in Fig. 8e. The corresponding electromagnetic field enhancement maps at the resonance maximum for each feature are modeled and shown in Fig. 8f. The gap mode near 1100 nm produces the largest field enhancement that, importantly, is largely confined to the gap region. The quadrupolar mode near 600 nm also produces significant field enhancement in the gap region, while the interband feature and the multipolar mode produce electromagnetic field enhancements that are distributed to a much greater extent away from the gap region. Thus, while all of the absorbed photons at the different resonances will contribute towards the production of energetic carriers, leading to a broadband response from the ultraviolet through the near-infrared spectral range, the gap mode and the quadrupolar mode are expected to display the greatest spectroscopic evidence of non-thermalized electrons.

We can further describe this in terms of the equation for the HE-production rate [23,41]:

$$Rate_{\mathrm{HE}} = \frac{1}{4}\frac{2}{\pi^2}\frac{e^2E_{\mathrm{F}}^2}{\hbar}\frac{1}{(\hbar\omega)^3}\int_S |E_{\omega,\mathrm{normal}}|^2 ds, \quad (13)$$

where $E_{\omega,\,\mathrm{normal}}$ is the complex amplitude of the dynamic electric field normal to the surface and taken inside a NC, and the physical field is given by $E_{\mathrm{normal}} = \mathrm{Re}E_{\omega,\,\mathrm{normal}}$; the integral in Eq. (13) is taken over all surfaces of the nanostructure. If the structure includes different components made of different metals, one should sum up the contributions from the different parts. The rate of production of non-thermalized carriers, Eq. (13) is inversely proportional to the cube of the photon energy, as well as it being proportional to the square of the field normal to the metal surface. Both factors directly favor the gap mode with its near-infrared resonance and high field enhancement at the metal-dielectric interface in the gap (which is also the case, although to a lesser extent, for the quadrupolar mode). It should also be pointed out that the lifetime of non-thermalized electrons is inversely proportional to the square of the photon energy, which also means that the longer lifetime at the gap mode resonance leads to a larger population build-up of non-thermalized carriers. All of these factors should be considered when designing metamaterial structures for hot carrier production.

The ultrafast transient absorption kinetics at each resonance are plotted in Fig. 8g. The ultrafast feature in the first few hundred femtoseconds is assigned to the presence of non-thermalized electrons. It is clear from the kinetics that the gap mode produces a very strong signature through non-thermalized electrons, although the quadrupolar mode also shows evidence of the excitation of non-thermalized electrons. Fig. 8h presents a diagram of the electronic populations excited in the gap mode, depicting the initial excited carrier distribution containing non-thermalized electrons and the subsequent thermalized picture, showing the dominant relaxation process in each instance. We emphasize that without the gap structure, e.g. nanocubes on a glass substrate, these features do not appear under any illumination condition. The other resonances involving the interband resonance and the multipolar mode show more conventional decay dynamics, similar to an isolated nanocube. We have globally analyzed this data, gathering evidence for the existence of 3 populations of hot carriers, and have proposed a degree of anisotropy in the decay of non-thermalized carriers [23], in what continues to be an active area of research.

Finally, we have also begun a critical step towards achieving the direct extraction of the hot electron distribution from ultrafast pump-probe spectra through a “double inversion” procedure [70]. This is done by solving (inverting) the equation that relates the time-resolved reflectivity data to the imaginary component of the metal’s complex dielectric function. This is followed by a second “inversion” to relate the imaginary component of the dielectric function to the occupancies of the single electron energy band. This effort has successfully produced hot electron energy distributions as a function of time in thin gold films under different illumination conditions, although additional research is required to extend this approach to more complex structures and metamaterials.

## Kinetic multi-temperature models

In the kinetic models available in the literature, one can find several useful approaches for describing the optically-excited Fermi gas in a metallic NC. In particular, one can recognize a few types of excited carriers and non-equilibrium temperatures, which appear in different regimes:

1) **Plasmonic (Drude) electrons** in a nanocrystal under CW light illumination [41]. These electrons constitute the plasmonic wave and its associated coherent electron currents, $\delta n_{\mathrm{Drude}}(\varepsilon)$. In large NCs, the distribution of these electrons resembles a thermal one because, as long as we assume a weak pumping regime, they are excited near the Fermi level. Along with the excited Drude electrons, an optically-driven NC includes, of course, **thermalized excited electrons**, $\delta n_T(\varepsilon)$ because such a NC has an increased lattice temperature. The first section and Fig. 2c,d described such non-equilibrium carriers (Drude and thermalized) using the distribution function coming the Boltzmann kinetic equation. For the steady-state regime with an oscillating plasmonic wave, one can introduce a useful parameter that can be regarded as **an effective electronic temperature,** $T_{\mathrm{e,eff}}$. This parameter simply describes an increase in the time-averaged electronic kinetic energy stored in the electron gas under CW excitation. For this we can use the equation

$$\int_0^\infty \varepsilon\delta n(\varepsilon)d\varepsilon = E_{\mathrm{EFG}}(T_{\mathrm{e,eff}}),$$

where $\delta n(\varepsilon)$ is the energy distribution of excited electrons in the plasmonic wave in the CW regime and $E_{\mathrm{EFG}}(T)$ is the total kinetic energy of the electron Fermi gas in equilibrium at temperature $T$.
2) **Non-thermalized energetic (hot) electrons** with excitation energies $\sim\hbar\omega$. For optical photons, $\hbar\omega\sim$2 eV, the effective temperature of such carriers, if calculated with the equation $\hbar\omega = k_{\mathrm{B}}T_{\mathrm{eff}}$, is ~20 000 K. Clearly, these are very energetic carriers that cannot be easily produced under the other regimes described below. The corresponding parameter for the non-thermalized HEs is simply the number of such carriers, $N_{\mathrm{HE}}$.
3) **Thermalized energetic (hot) electrons** appearing in nonlinear experiments with short fs-pulses. Such carriers appear after a fast relaxation process, due to e-e collisions in the electron gas,

decay kinetics of the gap plasmon and quadrupolar modes. **(h)** Illustration of the relaxation processes for hot electrons (left) and thermalized electrons (right), representing the general shape of the excited carrier population distributions for the gap mode at the times indicated by the dashed lines and the red and blue arrows underneath the data in panel (f). Panels (a)-(g) were reproduced with permission from [23]. Copyright 2017 Springer Nature.

which reduces the kinetic energy of the non-thermalized hot electrons. This relaxation time is very short because of the large e-e scattering rate, or cross section. The corresponding parameter in these models is the **effective electronic temperature** of the thermalized Fermi gas, $T_{e,eff}$, and it can be as high as a few thousand Kelvin [12,20].

4) The third parameter is the **lattice temperature**, $T_L$. The hot thermalized electronic gas will tend to equilibrate its effective temperature with that of the lattice via electron-phonon scattering. Given the additional energy accumulated in the electron gas, the electron-phonon interaction represents a relaxation channel for the excited electrons.
5) Lastly, we should also account for the temperature of the matrix, or **ambient temperature**, $T_0$. A NC in an excited vibrational state or, equivalently, hosting a phonon gas at a higher temperature than its surroundings, will tend to lose energy in favor of its environment, increasing $T_0$ via heat transfer.

Using the above dynamic parameters, one can now formulate **the extended 2T model** as a set of equations. Ref. [12] gives a good description for this model, and we will follow it below. To extend it, one can formulate a more advanced model such as the one that we present immediately afterwards, and to which we refer as **quantum 2T model.** In the extended 2T model, all optical energy absorbed by a NC contributes to the excitation of non-thermalized HEs. In the case of our quantum 2T model, formulated in Ref. [41], there are two energy-pumping rates integrated into the extended 2T model equations: one for the thermalized HEs and another one for the non-thermalized HEs. The first rate is typically much larger and represents the classical effect of Drude-like excitation in the bulk. The second one comes instead from the interaction of the electrons in the plasmon wave with the surface, contributes to the generation of non-thermalized HEs and is a quantum effect.

a) **Extended two temperature (2T) model:** We now follow Ref. [12] and write the rate equations for the related energies, adding also an explicit coupling to the environment's temperature $T_0$:

$$\begin{aligned}\frac{dE_{HE}}{dt} &= -a_{e\text{-}e}E_{HE} + P_{abs}\\ \eta_e T_e\frac{dT_e}{dt} &= -G(T_e - T_L) + a_{e\text{-}e}E_{HE}\\ C_L\frac{dT_L}{dt} &= G(T_e - T_L) - C_L\frac{T_L - T_0}{\tau_{heat\ transfer}}\end{aligned} \tag{14}$$

We should note that we have followed a slightly different notation than that in Ref. [12]. In the above set of equations, the parameters are defined as follows:

$E_{HE} \equiv$ total energy of nonthermalized HEs in a NC

$T_e \equiv$ electronic temperature

$T_L \equiv$ lattice temperature

$T_0 \equiv$ ambient temperature

$a_{e\text{-}e} \equiv$ e-e relaxation rate of HEs

$P_{abs} \equiv$ classical optical energy absorption rate of a NC

$G \equiv$ e-ph relaxation rate of thermalized HEs

$C_e = \eta_e T_e \equiv$ electronic heat capacity of a NC

$C_L \equiv$ lattice heat capacity of a NC; $C_L >> C_e$

$\tau_{heat\ transfer} \equiv$ time of heat transfer NC → matrix;

typically this is the longest relaxation time

and one can find realistic estimates for them in Ref. [12]. For confined systems, theheat exchange between a nanocrystal and its environment in both CW and pulsed illumination regimes is essential. For simplicity, we described here this process with the simplest, rate-equation approach (see the last equation in Eqs. (14)), which is widely used in the experimental literature [71]. In the CW regime, heat accumulates in a NC as the phononic energy of the lattice, and the steady-state phototemperature should be carefully evaluated from the energy balance equations (Eqs. (14)). Characteristic values for $\tau_{heat\ transfer}$ can be found in Ref. [38] and in Table S2 in Supporting Information.

b) **Quantum 2T (Q2T) model:** In this model, we follow the ideas presented in Ref. [34], where the process of absorption was divided in two parts: the generation of low-energy (Drude) electrons and non-thermalized HEs. Then, the system of Eq. (14) is simply rewritten as:

$$\begin{aligned}\frac{dE_{HE}}{dt} &= -a_{e-e}E_{HE} + P_{HE}\\ \eta_e T_e\frac{dT_e}{dt} &= -G(T_e - T_L) + a_{e\text{-}e}E_{HE} + P_{abs}\\ C_L\frac{dT_L}{dt} &= G(T_e - T_L) - C_L\frac{T_L - T_0}{\tau_{heat\ transfer}}\end{aligned} \tag{15}$$

where the classical absorption rate (Drude model) is given by

$$P_{abs} = \langle\int_{NC} dV\,\mathbf{j}\cdot\mathbf{E}\rangle_{time} = \mathrm{Im}(\varepsilon_{Drude})\frac{\omega}{2\pi}\int_{NC} dV\,\mathbf{E}_\omega\cdot\mathbf{E}^*_\omega$$

with the dielectric function of metal being $\varepsilon_{Drude}$. The HE generation arises from the non-conservation of electronic momentum at the surfaces of a NC, and the corresponding rate should be derived from a quantum formalism [41]:

$$P_{HE} \approx \frac{1}{4}\frac{2}{\pi^2}\times\frac{e^2E_F^2}{\hbar}\frac{1}{(\hbar\omega)^2}\int_{S_{NC}}|E_{\omega,\mathrm{normal}}(\mathbf{r})|^2 ds$$

where $E_{\omega,\mathrm{normal}}$ is the projection of the electric field onto the surface's normal, as defined above, and it is taken at points inside the NC and immediately adjacent to the surface. In large NCs, $P_{abs} >> P_{HE}$ because $P_{HE}/P_{abs}\sim l_{mfp}/a_0 \propto 1/a_0$, with $a_0$ being the characteristic size of the NC, but for small NCs these contributions can be comparable [43,44]. Fig. 9 illustrates the quantum 2T model.

Eqs. (14) and (15) give a realistic description, but they are still simplified. In this simplest approach, we assumed that the non-thermalized HEs and HHs are distributed homogeneously across the energy intervals (see Figs. 3c, 4d and 9a). Non-thermalized HEs are located in the interval $E_F + \hbar\omega > \varepsilon > E_F$ and HHs are found in the $E_F > \varepsilon > E_F - \hbar\omega$. Then, the estimates for the total energy stored in the non-thermalized carriers and the e-e relaxation are

$$E_{HE}(t) \approx \hbar\omega\cdot N_{HE}(t), \quad a_{e\text{-}e} \approx 1/\tau_{\varepsilon,e\text{-}e}(\varepsilon = E_F + \hbar\omega/2)$$

where $N_{HE}$ is the number of HEs in the interval $E_F + \hbar\omega > \varepsilon > E_F$ and the e-e relaxation time $\tau_{\varepsilon,e\text{-}e}(\varepsilon)$ is given in Supporting Information. The energy for the relaxing HE was taken in the middle of the distribution interval at $\varepsilon = E_F + \hbar\omega/2$. In Figs. 10–12, we however show the results from a more advanced theory based on the kinetic Boltzmann-like equation, described in Supporting Information. In this advanced quantum theory, we need to make the following substitutions in Eq. (15):

$$a_{e\text{-}e}E_{HE} \to Q_{HE}(t), \quad G(T_e - T_L) \to \frac{\eta_e}{2}\frac{(T_e^2 - T_L^2)}{\tau_{\varepsilon,\mathrm{phonons}}} \tag{16}$$

where $Q_{HE}(t)$ is defined in detail in Supporting Information, $\tau_{\varepsilon,\mathrm{phonons}}$ is the electron energy relaxation rates due to emission of phonons and $C_e = \eta_e T_e$ is the electronic heat capacitance.

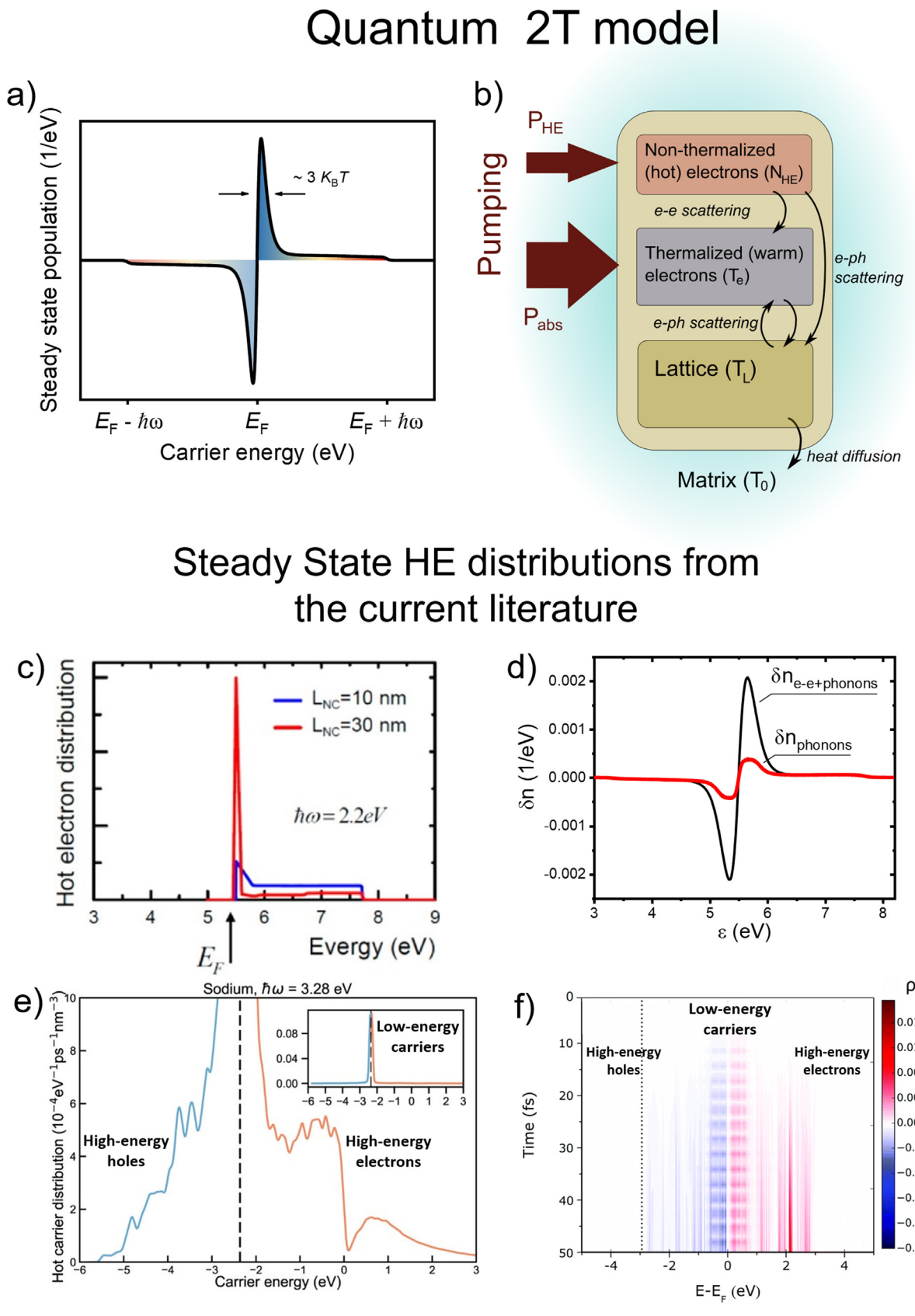


**Fig. 9.** Fundamentals of the quantum 2T model (Q2T). **(a)** Typical spectral profile for the generation of excited carriers under illumination in the Q2T model. There are two fundamental types of features in these data: a large number of warm (low-energy) carriers grouping at energies ~$3k_BT_e$ around $E_F$, and a shallow plateau of hot carriers with energies up to $\hbar\omega$ from $E_F$. **(b)** Diagram showing the different energy repositories in the system and the interactions that exchange energy between them. Crucially, the Q2T model differs from the traditional extended 2T model in that light excites both hot and warm electrons, as opposed to initiating a downward cascade with the hot electrons. Panels c to f present steady-state excited carrier populations in plasmonic nanocrystals, obtained with different formalisms and parameters. **(c)** Steady-state hot electron distribution for gold nanocubes with sizes of 10 nm and 30 nm, normalized by their respective volumes [72]. Smaller nanoparticles generate a greater proportion of

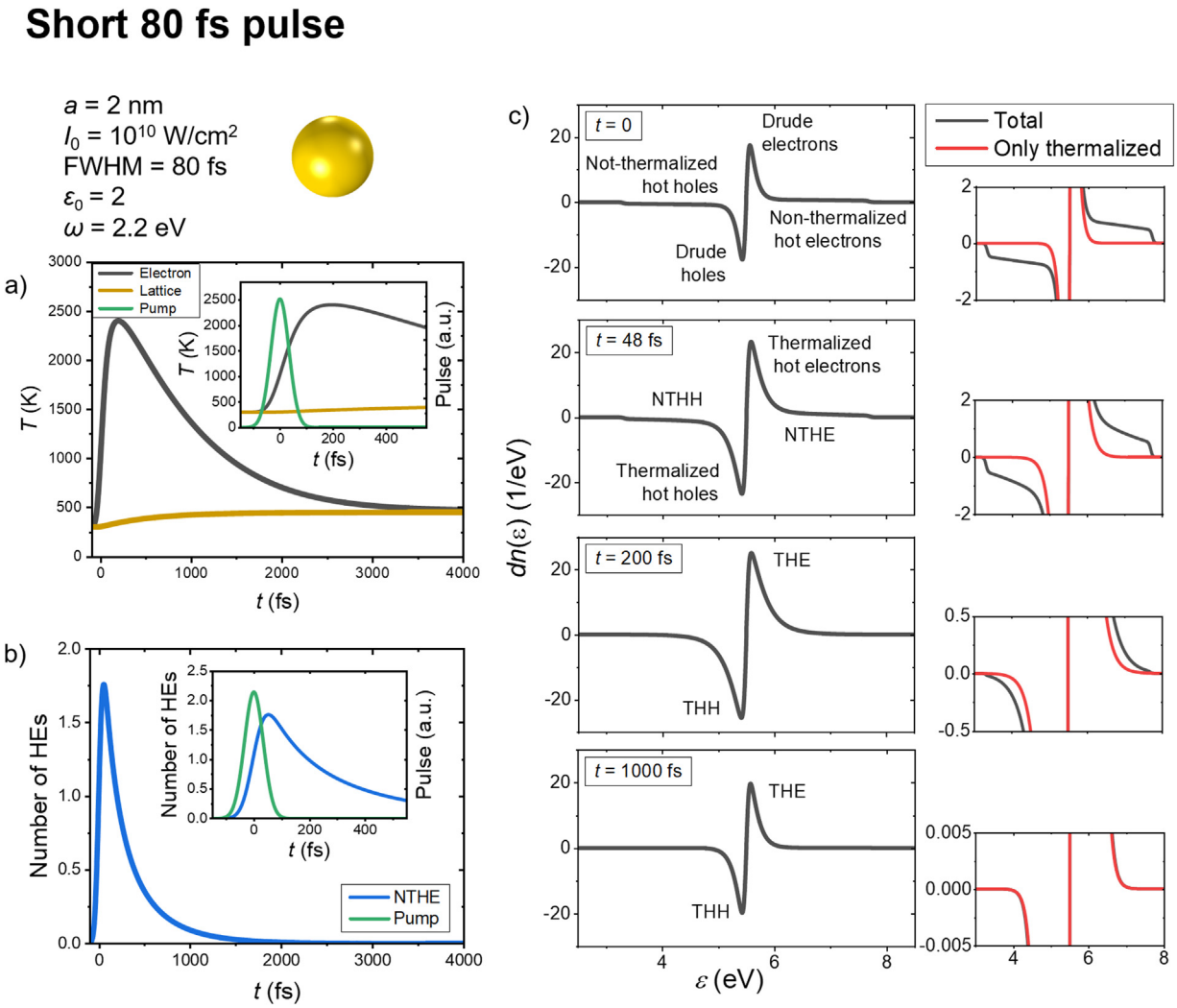


**Fig. 10.** Kinetics of a small gold plasmonic NP of 2 nm, prompted by the excitation of an 80-fs pulse centered at t = 0, obtained with our Q2T model. The inset on top shows the geometry of the NP, next to the relevant physical parameters of the system and excitation. **(a)** Time evolution of the effective temperatures of the electron gas and the metal lattice, with the inset highlighting the changes at short times after the pump pulse, also depicted there. It can be seen how the relevant timescales for the changes in $T_e$ and $T_L$ are very different, and how they equilibrate at long times as the electrons share their energy with the phonon gas in the metal. **(b)** An equivalent representation of the remaining parameter in an extended 2T model, the number of non-thermalized HE, $N_{HE}$. We can see how the characteristic relaxation time is shorter than that of the thermalized HE. **(c)** Four snapshots at different times of the non-equilibrium changes in carrier population induced by the pulse. The larger panels, on the left, show the total energy-resolved changes in the carrier population, while the smaller ones, on the right, zoom in to highlight the distinction between the total excited carrier density and the thermalized HEs. The difference between these curves is, of course, due to the presence of non-thermalized HEs, which we can see rapidly disappearing as they thermalize and increase the effective electron temperature.

Finally, we should mention that both models in Eqs. (14),(15) are formulated in terms of incoherent electronic and phononic excitations. The above assumes that the coherent plasmonic excitations have the shortest lifetime as compared to the other relaxation time scales. This is fully consistent with the known properties of these phenomena, whose relevant time scales are summarized in Fig. 4d.

The striking property of the calculations of steady-state distributions of excited carriers is the presence of a relatively small number of non-thermalized HEs in NCs with sizes of a few nanometers and larger. Fig. 9a illustrates the typical situation found for NCs with sizes ~2–3 nm [41]. There are two major reasons for this: (1) the generation of the non-thermalized HEs with large energies is a surface effect and, for the NCs with sizes with a well-developed plasmon peak, the number of high-energy electrons will always be small; (2) the very fast relaxation occurring by e-e scattering for energetic electrons in the Fermi sea greatly diminishes the steady-state populations of carriers with high energies.

hot electrons per unit of volume, while larger nanocrystals favor the generation of low-energy plasmonic carriers. **(d)** Distribution of excited carriers in a 4 nm gold nanoparticle excited at $\hbar\omega = 2.2$ eV, comparing the results derived from assuming only phonon-assisted electron scattering versus a model also including electron-electron scattering. The introduction of electron-electron scattering greatly decreases the lifetime of high-energy carriers, thus shifting the ratio between hot and warm electrons in favor of the latter [41]. **(e)** Excited carrier distribution in a Na particle of 10 nm, where the carriers' energy is referenced with respect to the vacuum level and the Fermi energy is marked by the vertical dashed line. The inset shows the full dataset, from which it is clear that the great majority of excited carriers accumulate around the Fermi energy [73]. **(f)** Time evolution of the electronic population in an icosahedral silver nanocluster of 3.3 nm, excited at $\hbar\omega = 2.885$ eV. Note the rise of population in the states around the Fermi energy, and the ultrafast subsequent population of high-energy states, with a delay consistent with the lifetime of the plasmon. The vertical dotted line mark the start of the d-band [74]. Reproduced with permission from (c) [72] Copyright 2013 American Chemical Society, (d) [41] Copyright 2017 American Chemical Society, (e) [73] Copyright 2018 American Chemical Society, (f) [74] Copyright 2019 Royal Society of Chemistry.

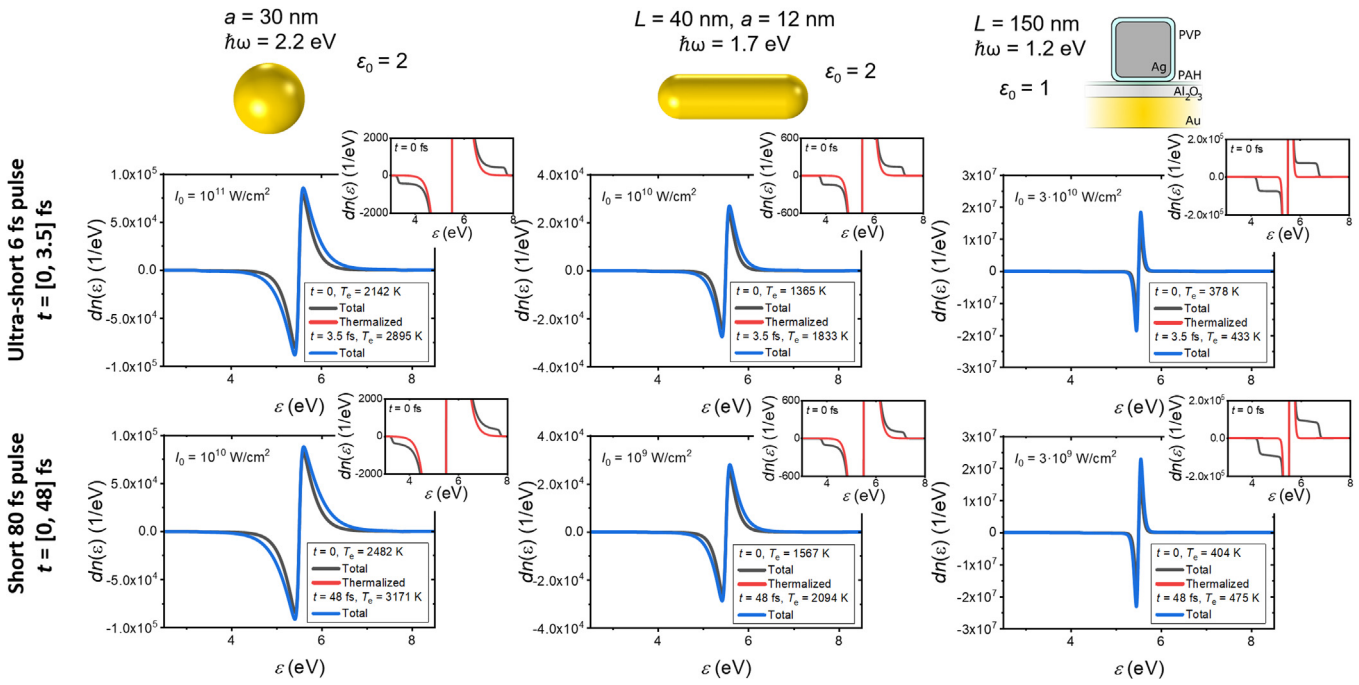


**Fig. 11.** Spectra of carrier populations for different plasmonic systems, generated by excitation with a pumping pulse centered at t = 0, obtained with our Q2T model. The three columns separate the results for the three different geometries, depicted on the top alongside the numerical details of the calculations. The two rows of panels relate to the length of the excitation pulse, with the top row corresponding to the ultra-short pulse of 6 fs and the bottom row corresponding to an 80 fs pulse. Now, each panel presents the following data: the non-equilibrium total carrier populations at two distinct times ($t = 0$, or at the pulse center, and shortly after the end of the pulse), with the legends noting the effective temperatures of the electronic gas at these times. Each panel also includes a small inset with the distinction between THE carriers and the total distribution at $t = 0$. A comparison across the three geometries in this figure evidences that the ratio of non-thermalized HEs to the thermalized ones is higher for the metasurface (see Fig. 12). The geometrical parameters of the metastructure are taken from Ref. [23].

Fig. 9c–f shows four examples of HE distributions from the current literature, which are based on different formalisms and relaxation parameters; we can see that the low-energy electrons dominate the picture [41,72–75]. In Refs. [41,72], it was found that these low-energy electrons are simply the electrons forming the plasmon oscillation and induce the dissipation described by the Drude model. Therefore, such excited carriers can be regarded as Drude electrons. Other important factors are, of course, the optical scattering phenomenon and the related electromagnetic field patterns in a nanostructure [76–78].

At this point, we will present some results obtained from the Q2T model, as described in Eq. (15) and extended in Supporting Information. Overall, we observe a relatively small number of non-thermalized HEs, because of two fundamental reasons: (1)

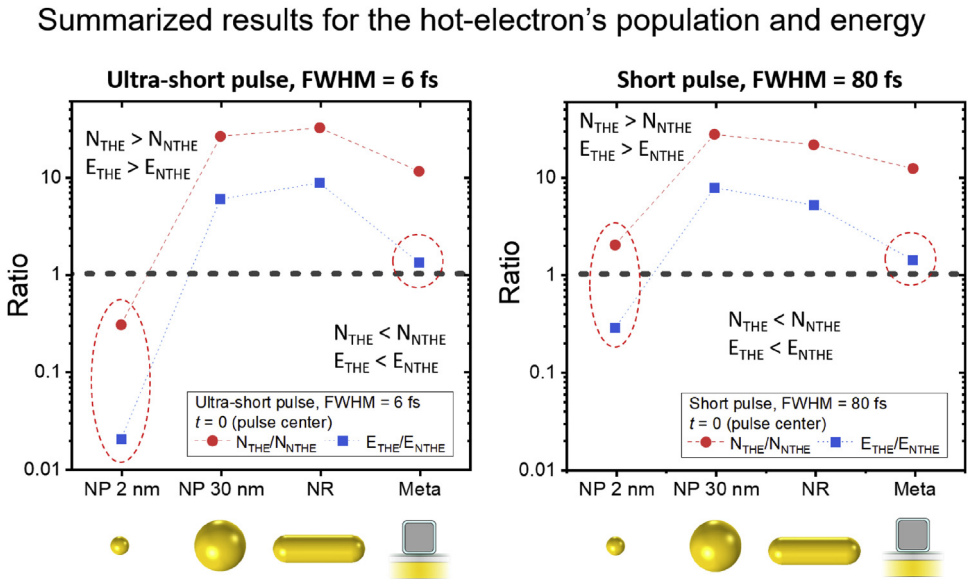


**Fig. 12.** Summary of results obtained with the Q2T model for different plasmonic systems (Figs. 10,11). Both panels show the ratios of two integrated variables (number of electrons, $N$, and total energy stored in them, $E$) between thermalized (THE) and non-thermalized (NTHE) hot electrons. The left panel corresponds to non-equilibrium populations existing in the middle of a pump pulse of 6 fs in duration, while the right one shows the equivalent data for an 80 fs pulse. The relative importance of non-thermalized hot electrons is highest for the small NPs and the metamaterial, as the datapoints highlighted by circles show.

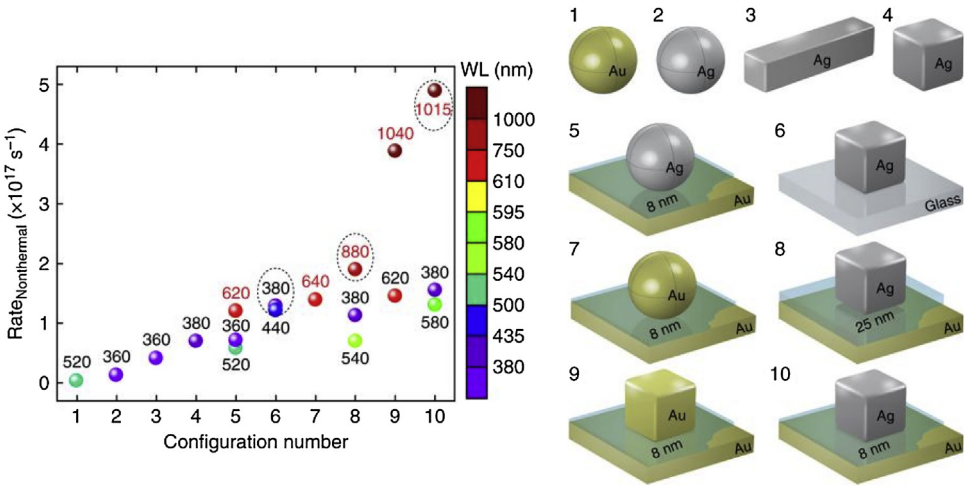


**Fig. 13.** Summary of theoretical data on the HE electron generation for a variety of different nanocrystals and metastructures. The color legend and the numbers next to the data points show the plasmon wavelength, and the configuration number indexes the particular systems under examination, depicted on the right. It is worth noting that the structures are arranged in order of increasing HE generation efficiency, with three factors accounting for greater excitation rates: (1) the presence of gap modes, (2) the use of NCs with sharper features, and (3) the use of silver NCs. The dashed circles highlight the systems that were experimentally studied in Ref. [23] through pump-probe spectroscopy. Reproduced with permission from [23]. Copyright 2017 Springer Nature.

Highly-energetic HEs arise from the surface effect and (2) the e-e scattering is very probable, setting relaxation times as short as ~10 fs for the high-energy electrons. In Figs. 10,11, we see relatively small populations of high-energy HEs in nanostructures of all types. However, when we look at the energy stored in the thermalized and non-thermalized carriers, these can be comparable when using small-sized NCs and metastructures (Fig. 12). This is a general and fundamental property. Let us now describe Fig. 12 in more detail. In it we show the ratios $N_{\text{Thermalized HE}}/N_{\text{Non-Therm. HE}}$ and $E_{\text{Thermalized HE}}/E_{\text{Non-Therm. HE}}$, where $N_{\text{Thermalized HE}}$ and $N_{\text{Non-Therm. HE}}$ are the number of electrons of each type (values integrated over the relevant energy values, separated by $\varepsilon = E_F + 3k_BT_e$). $E_{\text{Thermalized HE}}$ and $E_{\text{Non-Therm. HE}}$ follow the same logic, but represent the total energy stored by each type of excited carriers. We note that, when calculating the energy, we include that of both electrons and holes, i.e. we compute the full energy required to excite this non-equilibrium distribution from the one in equilibrium. However, when we compute the number of excited electrons, we count only the excited carriers above the Fermi level. When either of these ratios is less than one, the non-thermalized carriers dominate the picture. The important observations here are: (1) Smaller NCs exhibit larger populations of non-thermalized HEs than thermalized electrons; and (2) metastructures with hot spots in the infrared show strong generations of non-thermalized HEs, as described in the above section. According to Fig. 12, the non-thermalized carriers can dominate the excitation energy in small NCs (2 nm) and metastructures. The latter case emphasizes the importance of hot spots for photochemistry, which was well described and emphasized in Ref. [40].

Another example of calculations of non-thermalized electrons in various metastructures can be found alongside experimental data in Ref. [23]. Various geometries were examined, and it was found that these type of metastructures generate HEs much more efficiently than any single, non-interacting NC (Fig. 13). In addition, it was found that the best performance corresponded to the metastructure with a silver nanocube on top of the Au-spacer substrate, which is reasonable if we remember that silver has a longer electronic mean free path than gold [41].

c) **Examples of experimental HE distributions:** Probing a distribution of HEs, both thermalized and non-thermalized, is an interesting and challenging task. Here we look at two recent examples of such type of studies. The first example, in Ref. [70], concerns the probing of changes in charge carrier population produced by a pump pulse in the infrared, exciting intraband plasmonic transitions in thin Au films. These are obtained by measuring the transient changes in the reflection of a probe pulse in the visible spectrum, which targets the interband transitions in gold (Fig. 14a). Supporting the physical perspective presented by the Q2T model, the distributions were never flat in the whole regions $E_F - \hbar\omega < \varepsilon < E_F$ and $E_F < \varepsilon < E_F + \hbar\omega$, contrary to how they are typically depicted in the literature (Fig. 7d,e). The measured distributions tend to concentrate near the Fermi energy, and for times comparable with the pulse length they resemble our data in Figs. 10,11. The widths of the distributions in Fig. 14a indicate that the HEs have large non-equilibrium temperatures. Another example of energy-resolved spectroscopy of plasmonic HEs concerns the energy distributions of electrons injected from Au NCs into a $TiO_2$ contact [79]. In this case, the authors of Ref. [79] measured the change in X-ray absorption in $TiO_2$ due to the HE injection from the plasmonic NC (Fig. 14b). Their results support the conclusion that the distribution of HEs in $TiO_2$ is highly non-thermal and originates from the injection of non-thermal electrons in the metal, which occupies the energy interval $0 < \varepsilon < E_F + \hbar\omega_p$, where $\hbar\omega_p$ is the plasmon energy (Fig. 14b). We expect such occupation spectrum, since the injected carriers are basically the plasmon-excited HEs from gold. In this case, the Au-$TiO_2$ Schottky barrier played the role of a detector, probing the distribution of HEs in the metal. These selected works are two recent examples of energy-resolved HE spectroscopy, realized with purely solid-state optoelectronic systems. However, we should also point out that chemical HE-driven photo-reactions utilizing NCs with various shapes also have the potential of implementing setups for energy-resolved spectroscopy [60].

## Plasmon-assisted tunneling, nonlinear photoemission and the Keldysh parameter

Up to this point in the review we have paid close attention to the fundamental processes and dynamics underlying the excitation of charge carriers in plasmonic nanoparticles. We have done this with the general goal of taking advantage of hot electrons in

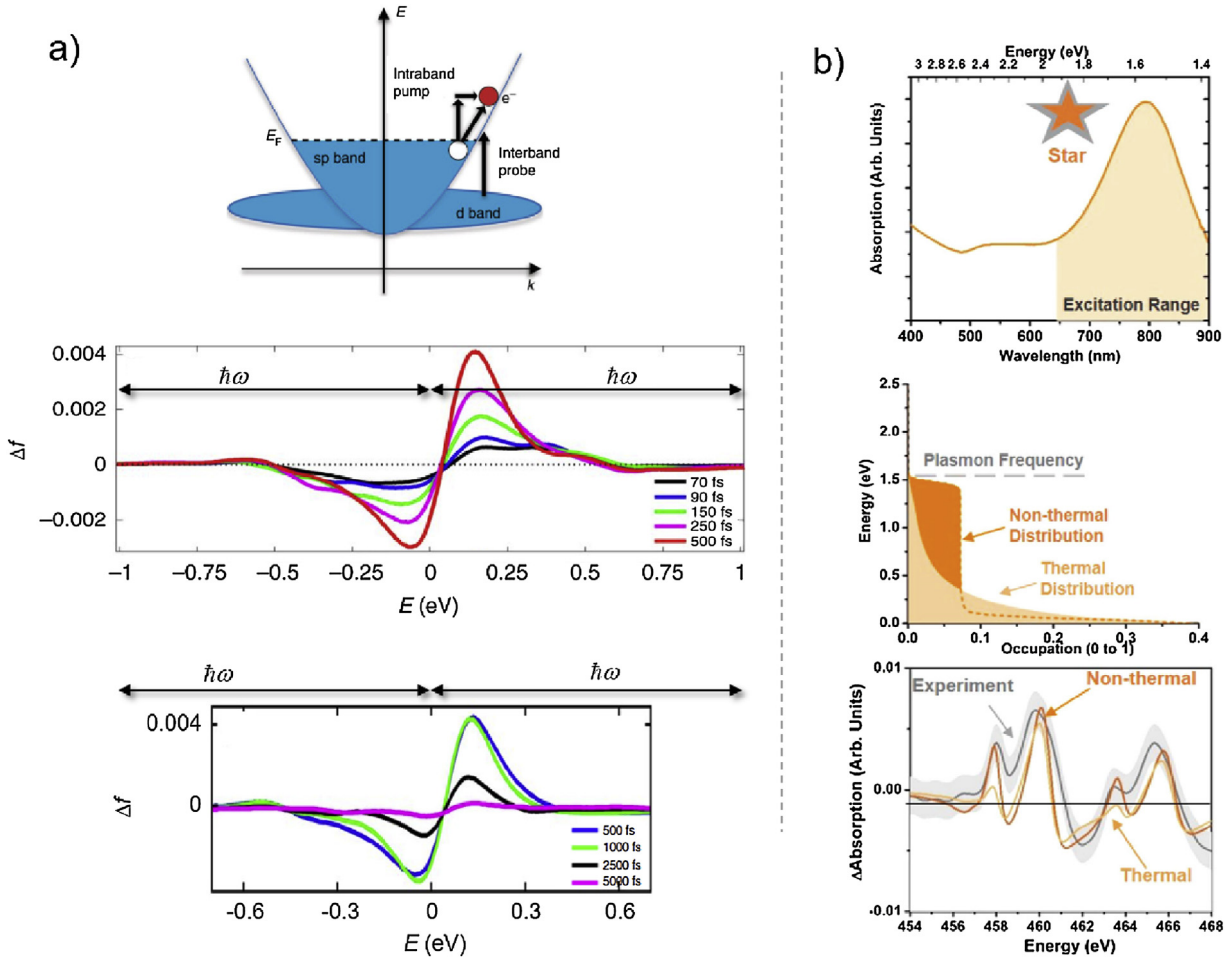


**Fig. 14.** Experimental techniques probing distributions of high-energy carriers. **(a)** (top) Diagram illustrating the band structure for gold, and the two types of transitions used in the pump-probe experimental setup; the other two panels show the energy-resolved excited carrier distribution in thin Au films, obtained from the analysis of reflectivity data in the visible spectrum, for short (middle panel) and longer (bottom panel) delays after illuminating the sample with a 130 fs pump pulse in the infrared [23]. The bars show the energy of the photon quanta used to excite the plasma. We can see, as predicted by the quantum 2T model [41,51,72], that the excited carriers are concentrated in energy near the Fermi level. The experiment in Ref. [23] is probably the only one in the current literature in which the detailed structure of the energetic carrier distribution is revealed. **(b)** The three panels refer to data corresponding to star-shaped core-shell Au@$TiO_2$ nanoparticles; (top panel) absorption data for the star nanoparticles, highlighting the spectral range that contributed to the plasmon excitation; (middle panel) theoretical data corresponding to the predicted thermal and non-thermal steady-state electron distribution at the nanostars; (bottom panel) experimental changes in X-ray absorption in the $TiO_2$ and two theoretical predictions, each assuming either a thermal or non-thermal distribution of carriers as the cause of the absorption changes, allowing a comparison that supports the latter hypothesis [79]. Reproduced with permission from (a) [23] Copyright 2018 Springer Nature and (b) [79] Copyright 2018 American Chemical Society.

driving different processes of scientific and technological import, such as photocatalysis and photodetection. Of course, most of the applications using high-energy charge carriers will depend on their extraction from the plasmonic system to drive the secondary physical processes that mediate the energy harvesting, signal processing, etc. In this section, we will take a closer look precisely at the physics of the emission of these carriers out of the plasmonic system and their injection into adjacent media, with a focus on their relevance for the creation of optoelectronic systems to process information. A clear understanding of the injection mechanism will help rationalizing the design process of optoelectronic systems and will open the door to hybrid computing devices operating at ultrafast speeds.

Plasmonic effects can also enhance the electron emission from metal surfaces, for instance, in resonant plasmonic nanostructures such as bowtie antennas [80–83]. However, driving a DC unipolar current in such nanostructures requires a symmetry breaking of the spatio-temporal electron dynamics [84–86]. For nanostructures, this has been achieved by using few-cycle femtosecond pulses for the optical excitation [80,87], by applying strong DC electric fields at the emitter electrodes [81], or by utilizing asymmetric nanojunctions (Fig. 15a). An electrodynamic symmetry breaking also favors optical rectification processes, which are typically detectable at the lowest optical intensities for metallic nanostructures [88,89]. Karnetzky et al. demonstrated that the asymmetric nanojunctions can be designed such that the plasmonic enhancement is larger on the emitter side than on the collector (Fig. 15b) [86]. In turn, a phase-stable laser can give rise to a unipolar current of emitted hot electrons across the gaps from the emitter to the collector (Fig. 15c) [86]. Generally, such emission currents $I_{\text{emission}}$ follow a non-linear dependence vs the peak electric laser field $F_{\text{laser}}$ at zero bias (with the laser pulse energy $E_{\text{pulse}} \propto F_{\text{laser}}^2$) [80,86,90]. The non-linear photoemission processes can be described by the Keldysh theory [91].

$$I_{\text{emission}} \propto \exp\left(-\frac{2\Phi_{\text{barrier}}}{\hbar\omega}\left[\left(1+\frac{1}{2\gamma^2}\right)\operatorname{arcsinh}(\gamma)-\frac{\sqrt{1+\gamma^2}}{2\gamma}\right]\right),$$

with $\Phi_{\text{barrier}}$ the barrier height (in eV), $\hbar\omega$ the photon energy, and $\gamma$ the Keldysh parameter (blue line in Fig. 15d). The Keldysh parameter $\gamma$ is defined as

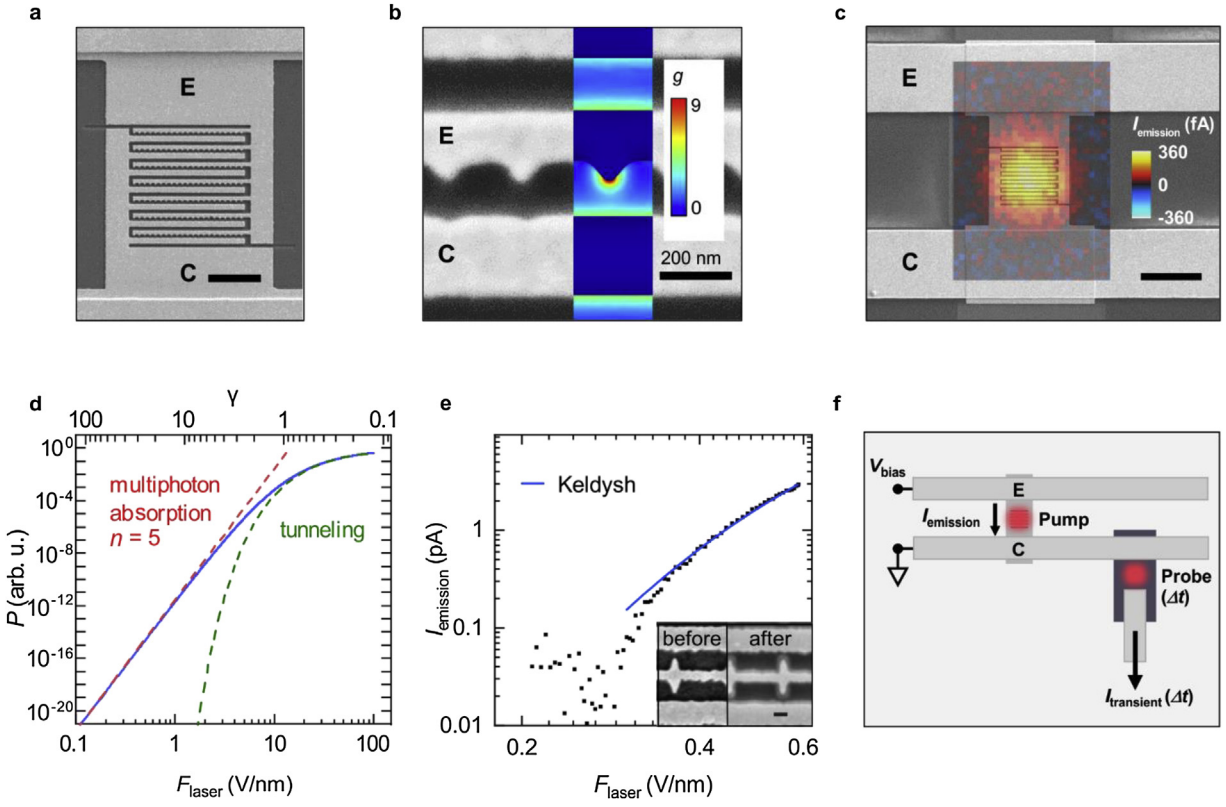


**Fig. 15.** Ultrafast electronics based on plasmonically enhanced photoemission of hot electrons. **(a)** Scanning electron microscope (SEM) image of Ti/Au contacts and asymmetric nanojunctions with the emitter (collector) denoted as 'E' ('C'). Scale bar, 2 μm [86]. **(b)** SEM close-up image with inset: numerically computed field enhancement $g$ within such an asymmetric nanojunction for a laser energy of 1.3 eV. **(c)** Lateral map of the unipolar photoemission current $I_{emission}$ at zero bias $V_{bias}$ across such asymmetric nanojunctions (overlaid plot), which are contacted by two Ti/Au striplines (outer SEM image). Scale bar, 5 μm. **(d)** Curve of the electron emission probability vs $F_{laser}$ according to the Keldysh theory (blue line) for a barrier height of gold $\Phi_{barrier} \approx 5.1$ eV and a laser energy $\hbar\omega \approx 1$ eV [90]. The corresponding Keldysh parameter $\gamma$ is displayed on the top axis. For low $F_{laser}$, the Keldysh curve approaches the multiphoton absorption (red dashed line), whereas for high $F_{laser}$, it is approximated by a tunneling probability (green dashed line). **(e)** $I_{emission}$ vs $F_{laser}$ (black dots). For large $F_{laser}$, the data can be fitted by the Keldysh curve (blue line), similar to the one shown in (d). Inset, left: High magnification SEM image of asymmetric nanojunctions before laser illumination. Inset, right: SEM image of the same junctions after laser illumination showing non-thermal gold ablation especially at the vicinity of the tips. Scale bar, 100 nm. **(f)** Schematic of an on-chip THz time-domain circuit with optical femtosecond pump and probe pulses triggering the electronic read-out. $I_{emission}$ describes the time-integrated photoemission current in the nanojunctions (as in c), while $I_{transient}$ captures the time-resolved electromagnetic transients in the striplines at a time delay $\Delta t$. Reproduced and adapted with permission from Refs. [86] and [90]. Copyright 2019 American Chemical Society and 2019 Springer Nature.

$$\gamma = \frac{\omega\sqrt{2m\Phi_{barrier}}}{eF_{laser}},$$

where $m$ is the electron mass, and $e$ the electron charge [91]. In the limit of low laser fields (Keldysh parameter $\gamma \gg 1$), the multiphoton absorption process dominates the emission current (dashed red line in Fig. 15d) [90,91], and the power law coefficient resembles the number of absorbed photons. For a work function of gold ($\Phi_{barrier} \sim 5.1$ eV) [92] and a laser energy of $E_{photon}$ = (0.9–1.3) eV and further parameters as in Refs. [86,90], 6 - 4 photons are involved according to this theory. For $\gamma \ll 1$, the emission current $I_{emission}$ can be described by the tunnel current (dashed green line in Fig. 15d)

$$I_{emission} \propto \exp\left(-\frac{2\Phi_{barrier}}{\hbar\omega}\frac{2\gamma}{3}\right)$$

which in principle, has the same exponential behavior as predicted for electron tunneling by the Fowler-Nordheim equation [93]. The theory by Keldysh neglects any ponderomotive quiver motions and further strong-field effects, as well as the effect of the carrier envelope phase during the photoemission process [80,94–97]. However, it allows considering plasmonic effects in a straightforward manner. In particular, Zimmermann et al. demonstrated that the spectrally averaged plasmonic enhancement of metallic nanojunctions can be simply multiplied to the expected emission current according to the far-field value of $F_{laser}$ [90]. They find effective plasmonic enhancement factors in the order of 10–30 (Fig. 15b) to explain the unipolar photoemission current across the nanojunctions for large $F_{laser}$ and plasmonic nanojunctions with a sub-10 nm gap-distance (blue line in Fig. 15e) [90]. Further screening effects explain the deviation at low $F_{laser}$. The inset of Fig. 15e demonstrates that the laser excitation of metallic nanojunctions can give rise to a non-thermal ablation processes forming such sub-10 nm gaps [90], which are promising for nanoelectronic applications of ultrafast, plasmonically enhanced photoemission currents, e.g. across single carbon nanotubes [98]. Further possible applications are on-chip THz-circuits (Fig. 15f) [86], where an ultrafast pump laser initiates the non-linear photoemission current $I_{emission}$ in asymmetric plasmonic nanojunctions, which are centered in-between two co-planar THz-striplines (Fig. 15c and f). The generated on-chip THz-pulse is detected as a transient current $I_{transient}$ in a semiconducting Auston-switch triggered by a probe laser at a time-delay $\Delta t$ [86,99,100]. Such on-chip THz-circuits allow femtosecond electron currents in the frequency range up to 10 THz.

## Life after the fast thermalization: Coherent phonon breathing oscillations

After the ultra-fast and fast relaxation processes in the electron-phonon system have taken place, we should still expect some

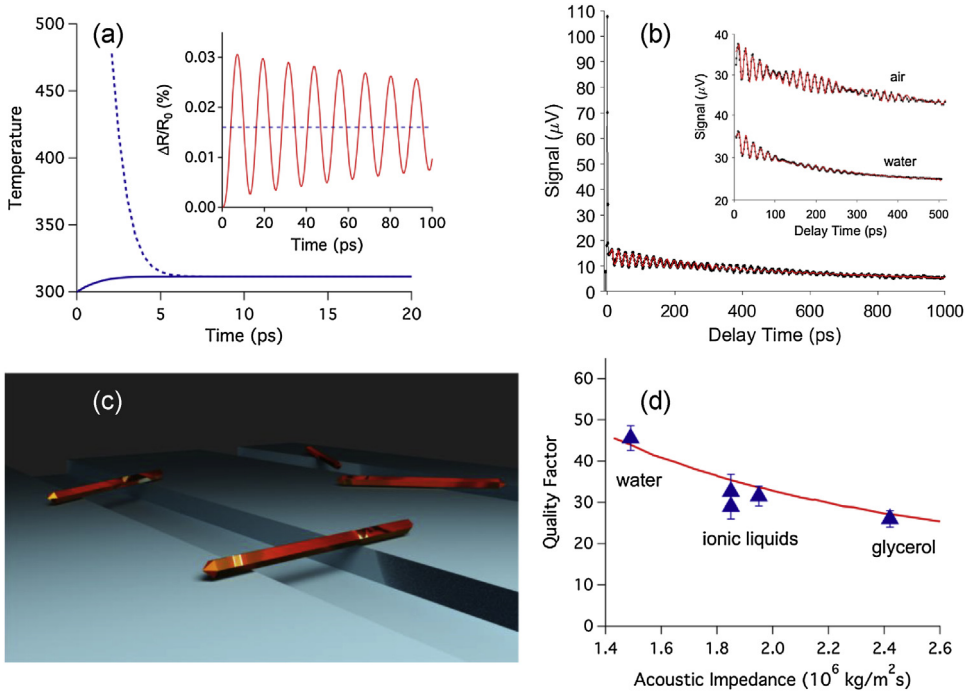


**Fig. 16.** Coherent vibrational modes in metal nanoparticles. **(a)** Calculation of the change in electronic and lattice temperature for a Au nanoparticle for an initial electronic temperature of 1000 K (dashed and solid lines, respectively). The inset shows the change in radius of a 20 nm diameter Au particle driven by the time dependent lattice temperature. **(b)** Transient absorption trace for a single, suspended Au nanowire in air. The insets show the modulated portion of the trace for the nanowire in air and water [109]. **(c)** Cartoon of the experimental geometry for the experiments in panel (b). **(d)** Quality factors for damping of the acoustic vibrational modes of Au nanowires in different liquids, plotted versus the acoustic impedance of the liquid. Points = experimental data averaged over many nanowires (errors are 95% confidence limits); line = calculations for the damping of the breathing mode of a cylindrical nanowire in a homogeneous solid-like environment. Reproduced with permission from (b) [109] Copyright 2018 PCCP Owner Societies, (c) [107] Copyright 2013 PCCP Owner Societies.

interesting, nontrivial phenomena. The ultrafast plasmon dephasing and electron-electron interactions discussed above create a distribution of hot electrons that can be described by a Fermi-Dirac distribution [17,101]. Because there has been very little energy exchange with the lattice on the sub-ps timescale of electron-electron coupling, the temperature of this distribution is much higher than the temperature of the phonon modes of the nanostructure [17,101]. The hot electrons will subsequently relax, and this relaxation process can be described using the two-temperature model [17,48,63,101,102]. In this model the electrons and lattice exchange energy in a way that depends on their temperature difference:

$$C_e(T_e)\frac{dT_e}{dt} = -g(T_e - T_L) \tag{17a}$$

$$C_L\frac{dT_L}{dt} = g(T_e - T_L) \tag{17b}$$

where $g$ is the electron-phonon coupling constant, $T_e$ and $T_L$ are the electron and lattice temperatures, and $C_e(T_e)$ and $C_L$ are the corresponding heat capacities [17,48,63,101,102]. Because the electronic heat capacity depends on temperature ($C_e(T_e) \propto T_e$) the time-constants for electron-phonon coupling depend on the excitation intensity in pump-probe measurements [48,103]. This means that very low pump laser powers should be used to measure $g$. Careful, low-power ultrafast measurements for Ag and Au nanoparticles have shown that the electron-phonon coupling constant for small particles is similar to that of the bulk metal down to ca. 5 nm diameter [104]. At smaller sizes there is an increase in the rate of electron-phonon coupling. This has been attributed to electron spill-out at the surface of the particles, which becomes important at small sizes [104].

The result of the electron-phonon coupling process is that heat flows into the lattice of the particles on a timescale of a few picoseconds, which will cause the lattice to expand [48]. The timescale for electron-phonon coupling is faster than the period of the acoustic vibrational modes of the particle that correlate to the expansion coordinate (the "breathing" modes of the nanostructure), which means that these modes can be coherently excited. Fig. 16a shows a simulation of the change in $T_e$ and $T_L$, and the associated change in radius for a 20 nm gold nanoparticle with an initial electronic temperature of 1000 K. After equilibration between the electrons and phonons the lattice temperature of the particle increases by 11 K, which causes a lattice expansion of 0.016%. The inset of Fig. 16a shows a simulation of the change in radius of the particle using a driven harmonic oscillator model [48]:

$$\frac{d^2R}{dt^2} + \frac{2}{\tau}\frac{dR}{dt} + \left(\frac{2\pi}{T_{br}}\right)^2\left\{R - R_0\left(1 + \frac{\alpha}{3}\Delta T_L\right)\right\} = 0 \tag{18}$$

where $\Delta T_L$ is the time-dependent change in lattice temperature that provides the driving force, $T_{br}$ is the period of the breathing mode, $\tau$ is the damping time, $R_0$ is the initial radius, and $\alpha$ is the coefficient of thermal expansion. The simulations show that the radius oscillates around the equilibrium radius of the hot particle (indicated by the dashed line in the figure). The amplitude of the oscillations is twice the change in radius due to heating – which is exactly the result expected for a displaced harmonic oscillator. The oscillations in the radius cause a small change in the volume of the particles, which shifts the plasmon resonance. This creates a signal in transient absorption experiments when the probe laser is tuned near the resonance [48,105,106].

Fig. 16b shows an example transient absorption trace for a single gold nanowire suspended over a trench. A cartoon of the experimental geometry is shown in Fig. 16c [107]. The signal shows a fast

decay, which corresponds to the electron-phonon coupling process, followed by modulations due to the breathing modes of the nanowire, which are more clearly seen in the inset of Fig. 16b). The nanowires in these experiments have pentagonal cross-sections and, thus, have two breathing modes – one corresponding to motion at the apexes of the pentagon and one corresponding to motion at the faces [107,108]. Analysis of the transient absorption traces yields the frequencies and damping times for the breathing modes of the nanowire. These quantities provide information about the elastic properties of the nanowire, and how energy is transferred from the nanowire into the environment [48,105–108].

The measured vibrational frequencies are typically in good agreement with continuum mechanics calculations [48,53,62,110,111], which means that the elastic properties of metal nanostructures are the same as the bulk material. On the other hand, the energy relaxation times are not as well understood. This situation is similar to that for the plasmon resonances of metal nanoparticles, where the resonance frequencies can be accurately calculated, but the dephasing processes (electron surface scattering, radiation damping and hot electron transfer) are still subjects of intense research [15,112–114]. In general, single particle measurements are needed to examine the dephasing processes. This is because in ensemble experiments the distribution of sizes and shapes in the sample causes an inhomogeneous decay, which overwhelms the contribution from the natural lifetime of the resonances [15,48,110].

A major focus of research at the University of Notre Dame in the past decade has been to use single particle transient absorption experiments to study how the environment affects the damping of the breathing modes of metal nanostructures [115]. These experiments are performed in two steps. First, transient absorption measurements are performed on suspended nanostructures in air to measure the rate of internal relaxation for the vibrational motion. The environment around the nanowire is then changed in some way (for example, by adding a liquid) and the experiments are repeated [107–109]. The results of the two measurements are then subtracted to determine the effect of the environment. The inset of Fig. 16b shows example transient absorption traces for a suspended Au nanowire in air and water [109]. Adding water to the sample increases the damping. Quantitative information about the effect of the liquid is obtained by subtracting the quality factors $Q_i = \pi\tau_i/T_i$ for the two traces ($Q_{liq}^{-1} = Q_{tot}^{-1} - Q_{air}^{-1}$). Note that working with quality factors removes the trivial size dependence in the damping times and periods [48].

A number of different liquids have been examined in these experiments covering a wide range of viscosities [109]. Fig. 16d shows the quality factors for liquid damping measured in our single nanowire experiments, plotted versus the acoustic impedance of the liquid. The quality factors range from $46 \pm 3$ for water, to $26 \pm 2$ for glycerol (errors equal 95% confidence limits). There is only a small change in the liquid damping quality factor going from water to glycerol, which is surprising considering that there is a three order of magnitude difference in the viscosities of these two liquids [109]. Indeed, calculations of the vibrational damping that include liquid viscosity (but not liquid *visco*elasticity) predict that the breathing modes should be almost completely damped for glycerol [108]. The reason for the higher than anticipated quality factors for glycerol is that the presence of viscoelasticity triggers an inviscid response in the liquid, that is, the liquid responds so that damping of the breathing modes occurs by simple radiation of sound waves into the environment [116]. The solid line in Fig. 16d shows the results from calculations for a cylindrical nanowire in a solid-like environment [107,111]. In this model the rate of damping simply depends on the difference in acoustic impendence $Z = \rho c_L$ between the nanowire and the surroundings, where $\rho$ is the density and $c_L$ is the longitudinal speed of sound [117,118]. These simple calculations are in excellent agreement with the experimental measurements, confirming that damping is controlled by radiation of sound waves into the environment. However, the situation is more complicated for vibrational modes that produce shear waves in the liquid, such as the extensional modes of nanorods. In this case the damping times are predicted to be very sensitive to the shear elastic properties of the liquid [116].

An important aspect of the experiments on the vibrational modes of plasmonic nanostructures is that the frequencies can very high. For example, a 20 nm thick Au nanoplate (which is a structure that can be easily fabricated by using either electron beam deposition or wet chemical synthesis) will have a breathing mode frequency on the order of 80 GHz [117,118]. Such high frequencies offer intriguing possibilities for vibrational cooling, and creating mechanical systems in their ground vibrational state ("quantum mechanical mechanical systems") [119,120]. Another interesting avenue of research for these systems is to determine how the internal damping of the vibrational modes of the nanostructures depends on parameters such as the crystal structure, the vibrational frequency, the presence of defects, and even the form of the vibrational mode. This is an area of research that has not been explored in depth to date.

## Outlook

Plasmonic HEs and their study using time-resolved spectroscopy bring not only interesting and novel fundamental science, but also ideas for potential applications. The great advantage of nanostructures and metamaterials lies in changing their shape to control the concentration and funneling of optical energies at both the micrometer and nanometer scales. Such localization of the electromagnetic field has been successfully applied in the study of time-dependent phenomena (Fig. 8 above), photochemistry using NCs of different shapes [60,121] (Fig. 17a,b) and HE nanoscopy [26,27,122] (Fig. 17c,d). In particular, the nanostar geometry in colloidal NCs looks very promising for HE-induced photochemistry [59,60,121]. The observation of anomalous ultra-fast carrier relaxation in metastructures is one example of a new phenomenon enabled by shaping a plasmonic nanogeometry [22,23], and that has also developed our understanding of the mechanisms affecting the generation of HEs. Beyond its fundamental interest, this has technological relevance because HEs are employed to drive various chemical reactions [40,55–57,123–126] and also for nano-localized surface chemistry (Fig. 17e,f) [28,29,127]. These energetic, optically-excited electrons are involved in interfacial charge transfer [24,25,128] which, alongside their related dynamics, is responsible for the operation of Schottky devices and any chemical solid-liquid interface. The current theoretical understanding of the mechanisms of generation of non-thermalized HEs is already at an advanced stage. **The ways to increase the number of non-thermalized HEs** in a plasmonic NC were formulated in Refs. [23,41,59]:

(1) The use of NCs with small sizes;
(2) Utilizing complex shapes with a larger surface area to volume ratio;
(3) Designing nanostructures with strong and/or extended electromagnetic hot spots;
(4) Constructing hybrid nanostructure architectures with plasmon resonances in the red and infrared regions.
(5) Using plasmonic materials with sharp plasmonic resonances; e.g., a silver NC generates more non-thermalized HEs than a gold one.

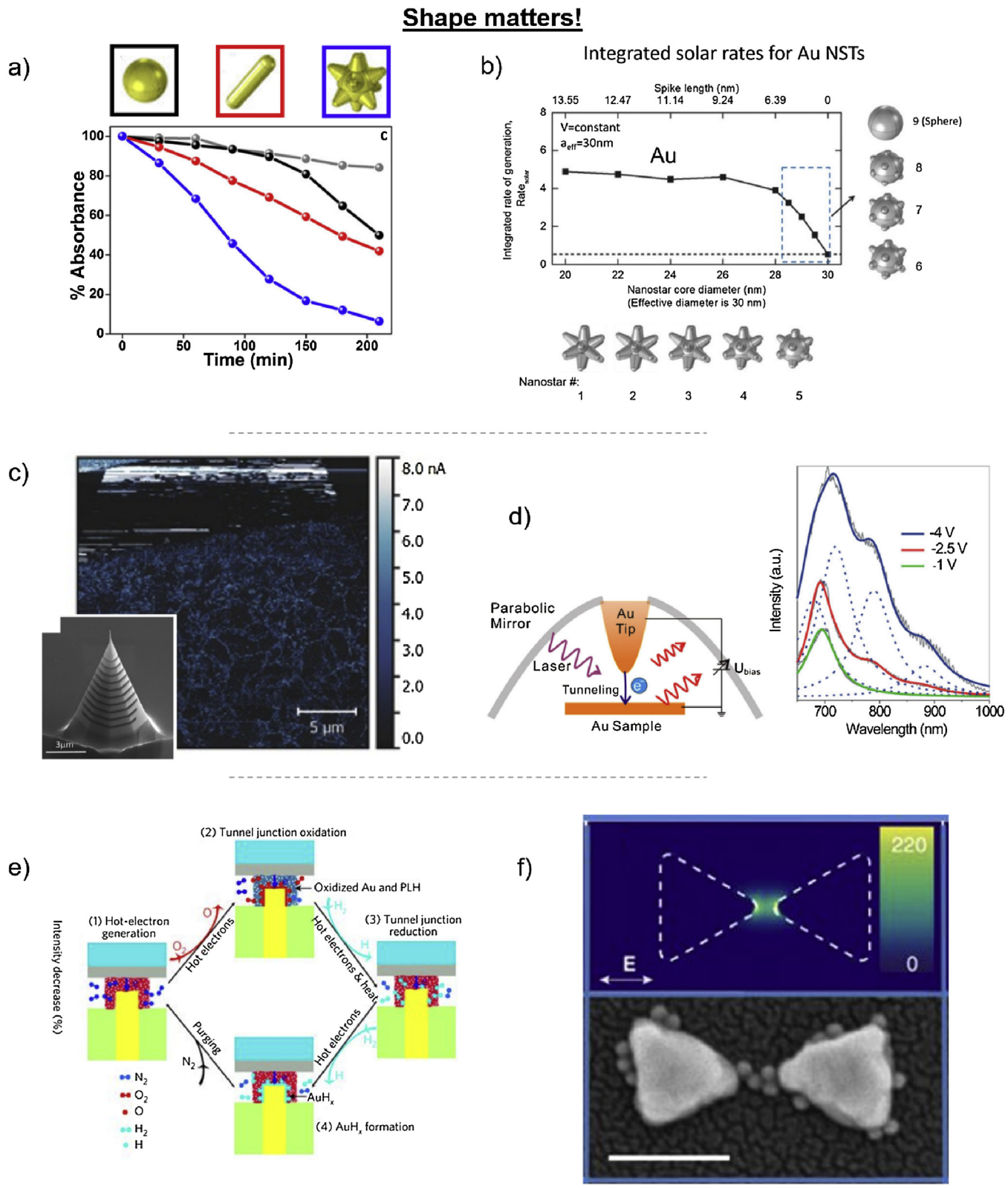


**Fig. 17.** Avenues for the development of applications based on plasmonic hot electrons. **(a)** Comparison of the photodegradation evolution of a dye in presence of $SiO_2$@$TiO_2$ and Au NCs of different shapes, where the nanostars outperform the other geometries and the reference data with no plasmonic NCs (grey curve) [60]. **(b)** Spectrally integrated hot electron generation for Au NCs with progressively shaper features, showing an increasing HE generation as the nanosphere develops into a nanostar [59]. **(c)** SEM of the AFM tip modified to perform HE-based scanning probe nanoscopy, over a map of current data obtained with this method at a $MoS_2$/SnO junction, showing the nanoscopic resolution of the technique [26]. **(d)** Scheme of a tip enhanced near-field optical microscope, used to study inelastic electron transfer at the tip-sample gap, with scence spectra obtained at different tip-sample bias voltages [27]. **(e)** Mechanisms affecting the chemical reactions in reactive tunnel junctions, where electrically-driven Au rods provide HEs and heat to activate the reactions [28]. **(f)** Simulated near-field (top) and SEM image (bottom) of a Ag bowtie antenna driving the HE-mediated reduction of its molecular coating; the aggregation of functionalized AuNPs is used to find the highly-active reaction sites of the antenna [29]. Reproduced with permission from (a) [60] Copyright 2016 American Chemical Society, (b) [59] Copyright 2017 Wiley, (c) [26] Copyright 2017 Wiley, (d) [27] 2015 Copyright 2015 American Chemical Society, (e) [28] Copyright 2018 Springer Nature, (f) [29] Copyright 2017 Springer Nature.

While the plasmon phenomenon is well described with classical theories, explaining the generation of HEs with high energies typically requires the use of quantum-mechanical and quantum-kinetic approaches. Therefore, future theoretical work on the physics and physical chemistry of HEs in the vicinity of interfaces described at the atomistic level, a field that is not developed enough yet, will require further development of these quantum models. In particular, such theories should be multi-scale, involving both DFT approaches (jellium-like and atomistic) and large-scale electromagnetic calculations based on Maxwell's equations. The DFT approaches would describe the microscopic quantum features, whereas the electromagnetic part of the modelling should provide us with the global picture of the plasmonic fields and related hot spots. Experimental methods and tools, which can reveal dynamic plasmonic properties at the interfaces, should include or combine optical spectroscopy and photo-chemical measurements. To name some, this review described two examples of advanced spectroscopic methods used to measure HE spectral distributions, namely fs pump-probe measurements and X-ray absorption spectroscopy [23,67,79]. This is, of course, not an exhaustive list, and many more methods, including photo-chemical approaches, could be named.

## Acknowledgments

L.V.B was supported by the Institute of Fundamental and Frontier Sciences, University of Electronic Science and Technology of China and China Postdoctoral Science Foundation (2017M622992). Z.W. was supported by National Basic Research Program of China (Project 2013CB933301) and National Natural Science Foundation of China (Project 51272038). A.W.H. acknowledges financial support of the Deutsche Forschungsgemeinschaft (DFG, German Research Foundation) under Germany's Excellence Strategy – EXC 2089/1 – 390776260. G.V.H. acknowledges the Support of the US National Science Foundation through Grant CHE-1502848. G.P.W. acknowledges support from the Center for Nanoscale Materials, a U.S. Department of Energy Office of Science User Facility under Contract No. DE-AC02-06CH11357. A.G. was funded via the 1000-talent Award of Sichuan and by the Volkswagen Foundation. Finally, A.G. holds the Chang Jiang (Yangtze River) Chair Professorship in China.

## Appendix A. Supplementary data

Supplementary material related to this article can be found, in the online version, at doi:https://doi.org/10.1016/j.nantod.2019.05.006.

## References

[1] S.M. Sze, K.K. Ng, Physics of Semiconductor Devices, John Wiley & Sons, Hoboken, NJ, 2006.
[2] A. Yariv, Optical Electronics, Saunders College Publ., Fort Worth, TX, 1991.
[3] C. Kittel, Introduction to Solid State Physics, 8th ed., John Wiley & Sons, Hoboken, NJ, 2004.
[4] J.D. Jackson, Classical Electrodynamics, John Wiley & Sons, New York, NY, 1998.
[5] H.C. van de Hulst, Light Scattering by Small Particles, Dover Publications, New York, NY, 1981.
[6] S.A. Maier, Plasmonics: Fundamentals and Applications, Springer, New York, NY, 2007.
[7] R.H.M. Groeneveld, R. Sprik, A. Lagendijk, Phys. Rev. B 51 (1995) 11433.
[8] S.I. Anisimov, B.L. Kapeliovich, T.L. Perel'man, Sov. Phys. JETP 39 (1974) 375–377.
[9] C.-K. Sun, F. Vallée, L.H. Acioli, E.P. Ippen, J.G. Fujimoto, Phys. Rev. B 50 (1994) 15337.
[10] M. Conforti, G. Della Valle,Phys. Rev. B 85 (2012), 245423.
[11] G. Della Valle, M. Conforti, S. Longhi, G. Cerullo, D. Brida,Phys. Rev. B 86 (2012), 155139.
[12] M. Zavelani-Rossi, D. Polli, S. Kochtcheev, A.-L. Baudrion, J. Béal, V. Kumar, E. Molotokaite, M. Marangoni, S. Longhi, G. Cerullo, P. Adam, G. Della Valle, ACS Photonics 2 (2015) 521–529.
[13] E. Carpene,Phys. Rev. B 74 (2006), 024301.
[14] T. Avanesian, P. Christopher, J. Phys. Chem. C 118 (2014) 28017–28031.
[15] A. Crut, P. Maioli, N. Del Fatti, F. Vallée, Chem. Soc. Rev. 43 (2014) 3921–3956.
[16] A. Arbouet, D. Christofilos, N. Del Fatti, F. Valle, J.R. Huntzinger, L. Arnaud, P. Billaud, M. Broyer,Phys. Rev. Lett. 93 (2004), 127401.
[17] C. Voisin, D. Christofilos, N. Del Fatti, F. Vallée, Phys. Rev. Lett. 85 (2000) 2200.
[18] H. Baida, D. Mongin, D. Christofilos, G. Bachelier, A. Crut, P. Maioli, N. Del Fatti, F. Vallée,Phys. Rev. Lett. 107 (2011), 057402.
[19] S. Link, M.A. El-Sayed, J. Phys. Chem. B 103 (1999) 8410–8426.
[20] M. Perner, P. Bost, U. Lemmer, G. von Plessen, J. Feldmann, U. Becker, M. Mennig, M. Schmitt, H. Schmidt, Phys. Rev. Lett. 78 (1997) 2192–2195.
[21] C. Sönnichsen, T. Franzl, T. Wilk, G. von Plessen, J. Feldmann, O. Wilson, P. Mulvaney, Phys. Rev. Lett. 88 (2002) 77402.
[22] H. Harutyunyan, A.B.F.F. Martinson, D. Rosenmann, L. Khosravi Khorashad, L.V. Besteiro, A.O. Govorov, G.P. Wiederrecht, L.K. Khorashad, L.V. Besteiro, A.O. Govorov, G.P. Wiederrecht, Nat. Nanotechnol. 10 (2015) 770–774.
[23] M.E. Sykes, J.W. Stewart, G.M. Akselrod, X. Kong, Z. Wang, D.J. Gosztola, A.B.F. Martinson, D. Rosenmann, M.H. Mikkelsen, A.O. Govorov, G.P. Wiederrecht, Nat. Commun. 9 (2017) 986.
[24] S. Tan, A. Argondizzo, J. Ren, L. Liu, J. Zhao, H. Petek, Nat. Photonics 11 (2017) 806–812.
[25] M. Taghinejad, H. Taghinejad, Z. Xu, Y. Liu, S.P. Rodrigues, K. Lee, T. Lian, A. Adibi, W. Cai,Adv. Mater. 30 (2018), 1704915.
[26] A. Giugni, B. Torre, M. Allione, G. Das, Z. Wang, X. He, H.N. Alshareef, E. Di Fabrizio,Adv. Opt. Mater. 5 (2017), 1700195.
[27] X. Wang, K. Braun, D. Zhang, H. Peisert, H. Adler, T. Chassé, A.J. Meixner, ACS Nano 9 (2015) 8176–8183.
[28] P. Wang, A.V. Krasavin, M.E. Nasir, W. Dickson, A.V. Zayats, Nat. Nanotechnol. 13 (2018) 159–164.
[29] E. Cortés, W. Xie, J. Cambiasso, A.S. Jermyn, R. Sundararaman, P. Narang, S. Schlücker, S.A. Maier, Nat. Commun. 8 (2017) 14880.
[30] M.R. Langille, J. Zhang, M.L. Personick, S. Li, C.A. Mirkin, Science 337 (2012) 954–957.
[31] Y. Zhai, J.S. DuChene, Y.-C. Wang, J. Qiu, A.C. Johnston-Peck, B. You, W. Guo, B. DiCiaccio, K. Qian, E.W. Zhao, F. Ooi, D. Hu, D. Su, E.A. Stach, Z. Zhu, W.D. Wei, Nat. Mater. 15 (2016) 889–895.
[32] D.B. Tanner, Optical Effects in Solids, Cambridge, England, Cambridge University Press, 2019.
[33] F. Wooten, Optical Properties of Solids, Academic Press, New York, NY, 1972.
[34] P.M. Platzman, P.A. Wolff, Waves and Interactions in Solid State Plasmas, Academic Press, New York, NY, 1973.
[35] C. Kittel, Quantum Theory of Solids, 2nd ed., Wiley, New York, NY, 1987.
[36] A.V. Chaplik, Surf. Sci. Rep. 5 (1985) 289–335.
[37] A. Marini, A. Ciattoni, C. Conti, Faraday Discuss. 214 (2019) 235–243.
[38] M. Hu, G.V. Hartland, J. Phys. Chem. B 106 (2002) 7029–7033.
[39] G.D. Mahan, Many-Particle Physics, Springer US, Boston, MA, 2000.
[40] P. Christopher, M. Moskovits, Annu. Rev. Phys. Chem. 68 (2017) 379–398.
[41] L.V. Besteiro, X.-T.T. Kong, Z. Wang, G. Hartland, A.O. Govorov, ACS Photonics 4 (2017) 2759–2781.
[42] M. Hu, C. Novo, A. Funston, H. Wang, H. Staleva, S. Zou, P. Mulvaney, Y. Xia, G.V. Hartland, J. Mater. Chem. 18 (2008) 1949.
[43] U. Kreibig, M. Vollmer, Optical Properties of Metal Clusters, Springer, Berlin, 1995.
[44] L. Genzel, T.P. Martin, U. Kreibig, Zeitschrift für Phys, B Condens. Matter Quanta 21 (1975) 339–346.
[45] Y. Zhang, C. Yam, G.C. Schatz, J. Phys. Chem. Lett. 7 (2016) 1852–1858.
[46] C. Sönnichsen, T. Franzl, T. Wilk, G. von Plessen, J. Feldmann, New J. Phys. 4 (2002) 93.
[47] J. Lermé, J. Phys. Chem. C 115 (2011) 14098–14110.
[48] G.V. Hartland, Chem. Rev. 111 (2011) 3858–3887.
[49] A.O. Govorov, H. Zhang, J. Phys. Chem. C 119 (2015) 6181–6194.
[50] M.J. Kale, P. Christopher, Science 349 (2015) 587–588.
[51] A.O. Govorov, H. Zhang, H.V. Demir, Y.K. Gun'ko, Nano Today 9 (2014) 85–101.
[52] G.V. Hartland, L.V. Besteiro, P. Johns, A.O. Govorov, ACS Energy Lett. (2017) 1641–1653.
[53] A. Crut, P. Maioli, N. Del Fatti, F. Vallée, Phys. Rep. 549 (2015) 1–43.
[54] A. Crut, P. Maioli, F. Vallée, N. Del Fatti,J. Phys. Condens. Matter 29 (2017), 123002.
[55] Y. Zhang, S. He, W. Guo, Y. Hu, J. Huang, J.R. Mulcahy, W.D. Wei, Chem. Rev. 118 (2018) 2927–2954.
[56] Q. Zhang, D. Thrithamarassery Gangadharan, Y. Liu, Z. Xu, M. Chaker, D. Ma, J. Mater. 3 (2017) 33–50.
[57] N. Wu, Nanoscale 10 (2018) 2679–2696.
[58] L.V. Besteiro, A.O. Govorov, J. Phys. Chem. C 120 (2016) 19329–19339.
[59] X.T. Kong, Z. Wang, A.O. Govorov,Adv. Opt. Mater. 5 (2017), 1600594.
[60] A. Sousa-Castillo, M. Comesaña-Hermo, B. Rodríguez-González, M. Pérez-Lorenzo, Z. Wang, X.-T. Kong, A.O. Govorov, M.A. Correa-Duarte, J. Phys. Chem. C 120 (2016) 11690–11699.
[61] A. Naldoni, U. Guler, Z. Wang, M. Marelli, F. Malara, X. Meng, L.V. Besteiro, A.O. Govorov, A.V. Kildishev, A. Boltasseva, V.M. Shalaev,Adv. Opt. Mater. (2017), 1601031.
[62] A. Crut, P. Maioli, N. Del Fatti, F. Vallée, Ultrasonics 56 (2015) 98–108.

[63] C. Voisin, N. Del Fatti, D. Christofilos, F. Vallée, J. Phys. Chem. B 105 (2001) 2264–2280.
[64] M.L. Brongersma, N.J. Halas, P. Nordlander, Nat. Nanotechnol. 10 (2015) 25–34.
[65] S. Mubeen, J. Lee, N. Singh, S. Krämer, G.D. Stucky, M. Moskovits, Nat. Nanotechnol. 8 (2013) 247–251.
[66] Z. Yin, Y. Wang, C. Song, L. Zheng, N. Ma, X. Liu, S. Li, L. Lin, M. Li, Y. Xu, W. Li, G. Hu, Z. Fang, D. Ma, J. Am. Chem. Soc. 140 (2018) 864–867.
[67] K. Wu, J. Chen, J.R. McBride, T. Lian, Science 349 (2015) 632–635.
[68] S. Mukherjee, F. Libisch, N. Large, O. Neumann, L.V. Brown, J. Cheng, J.B. Lassiter, E.A. Carter, P. Nordlander, N.J. Halas, Nano Lett. 13 (2013) 240–247.
[69] L. Yan, F. Wang, S. Meng, ACS Nano 10 (2016) 5452–5458.
[70] T. Heilpern, M. Manjare, A.O. Govorov, G.P. Wiederrecht, S.K. Gray, H. Harutyunyan, Nat. Commun. 9 (2018) 1853.
[71] D.K. Roper, W. Ahn, M. Hoepfner, J. Phys. Chem. C 111 (2007) 3636–3641.
[72] A.O. Govorov, H. Zhang, Y.K. Gun'Ko, J. Phys. Chem. C 117 (2013) 16616–16631.
[73] S. Dal Forno, L. Ranno, J. Lischner, J. Phys. Chem. C 122 (2018) 8517–8527.
[74] O.A. Douglas-Gallardo, M. Berdakin, T. Frauenheim, C.G. Sanchez, Nanoscale 11 (2019) 8604–8615.
[75] A. Manjavacas, J.G. Liu, V. Kulkarni, P. Nordlander, ACS Nano 8 (2014) 7630–7638.
[76] J. Codrington, N. Eldabagh, K. Fernando, J.J. Foley, ACS Photonics 4 (2017) 552–559.
[77] N. Zhang, C. Han, Y.-J.J. Xu, J.J. Foley, D. Zhang, J. Codrington, S.K. Gray, Y. Sun, J.J. Foley IV, D. Zhang, J. Codrington, S.K. Gray, Y. Sun, Nat. Photonics 10 (2016) 473–482.
[78] J. Zhang, X. Jin, P.I. Morales-Guzman, X. Yu, H. Liu, H. Zhang, L. Razzari, J.P. Claverie, ACS Nano 10 (2016) 4496–4503.
[79] S.K. Cushing, C.-J.J. Chen, C.L. Dong, X.-T.T. Kong, A.O. Govorov, R.-S.S. Liu, N. Wu, ACS Nano 12 (2018) 7117–7126.
[80] T. Rybka, M. Ludwig, M.F. Schmalz, V. Knittel, D. Brida, A. Leitenstorfer, Nat. Photonics 10 (2016) 667–670.
[81] W.P. Putnam, R.G. Hobbs, P.D. Keathley, K.K. Berggren, F.X. Kärtner, Nat. Phys. 13 (2017) 335–339.
[82] M. Aeschlimann, M. Bauer, D. Bayer, T. Brixner, S. Cunovic, F. Dimler, A. Fischer, W. Pfeiffer, M. Rohmer, C. Schneider, F. Steeb, C. Struber, D.V. Voronine, Proc. Natl. Acad. Sci. 107 (2010) 5329–5333.
[83] J. Kern, R. Kullock, J. Prangsma, M. Emmerling, M. Kamp, B. Hecht, Nat. Photonics 9 (2015) 582–586.
[84] L. Costa, M. Betz, M. Spasenović, A.D. Bristow, H.M. Van Driel, Nat. Phys. 3 (2007) 632–635.
[85] T. Higuchi, L. Maisenbacher, A. Liehl, P. Dombi, P. Hommelhoff, Appl. Phys. Lett. 106 (2015) 51109.
[86] C. Karnetzky, P. Zimmermann, C. Trummer, C. Duque Sierra, M. Wörle, R. Kienberger, A. Holleitner, Nat. Commun. 9 (2018) 2471.
[87] A. Schiffrin, T. Paasch-Colberg, N. Karpowicz, V. Apalkov, D. Gerster, S. Mühlbrandt, M. Korbman, J. Reichert, M. Schultze, S. Holzner, J.V. Barth, R. Kienberger, R. Ernstorfer, V.S. Yakovlev, M.I. Stockman, F. Krausz, Nature 493 (2012) 70–74.
[88] G.K.P. Ramanandan, G. Ramakrishnan, N. Kumar, A.J.L. Adam, P.C.M. Planken,J. Phys. D Appl. Phys. 47 (2014), 374003.
[89] D.K. Polyushkin, I. Márton, P. Rácz, P. Dombi, E. Hendry, W.L. Barnes,Phys. Rev. B 89 (2014), 125426.
[90] P. Zimmermann, A. Hötger, N. Fernandez, A. Nolinder, K. Müller, J.J. Finley, A.W. Holleitner, Nano Lett. 19 (2019) 1172–1178.
[91] L.V. Keldysh, J. Exp. Theor. Phys. 20 (1965) 1307–1314.
[92] D.E. Eastman, Phys. Rev. B 2 (1970) 1–2.
[93] R.H. Fowler, L. Nordheim, Proc. R. Soc. A Math. Phys. Eng. Sci. 119 (1928) 173–181.
[94] M. Schenk, M. Krüger, P. Hommelhoff,Phys. Rev. Lett. 105 (2010), 257601.
[95] M. Krüger, M. Schenk, P. Hommelhoff, G. Wachter, C. Lemell, J. Burgdörfer, New J. Phys. 14 (2012) 85019.
[96] G. Herink, D.R. Solli, M. Gulde, C. Ropers, Nature 483 (2012) 190–193.
[97] S.V. Yalunin, G. Herink, D.R. Solli, M. Krüger, P. Hommelhoff, M. Diehn, A. Munk, C. Ropers, Ann. Phys. 525 (2013) L12–L18.
[98] C. Karnetzky, L. Sponfeldner, M. Engl, A.W. Holleitner, Phys. Rev. B 95 (2017), 161405(R).
[99] D.H. Auston, IEEE J. Quant. Electron. 19 (1983) 639–648.
[100] D. Grischkowsky, I.N. Duling, J.C. Chen, C.C. Chi, Phys. Rev. Lett. 59 (1987) 1663–1666.
[101] N. Del Fatti, F. Vallée, C. Flytzanis, Y. Hamanaka, A. Nakamura, Chem. Phys. 251 (2000) 215–226.
[102] J.H. Hodak, I. Martini, G.V. Hartland, J. Phys. Chem. B 102 (1998) 6958–6967.
[103] J.H. Hodak, A. Henglein, G.V. Hartland, J. Chem. Phys. 112 (2000) 5942–5947.
[104] A. Arbouet, C. Voisin, D. Christofilos, P. Langot, N. Del Fatti, F. Vallée, J. Lermé, G. Celep, E. Cottancin, M. Gaudry, M. Pellarin, M. Broyer, M. Maillard, M.P. Pileni, M. Treguer, Phys. Rev. Lett. 90 (2003) 4.
[105] G.V. Hartland, Annu. Rev. Phys. Chem. 57 (2006) 403–430.
[106] G.V. Hartland, Phys. Chem. Chem. Phys. 6 (2004) 5263–5274.
[107] T.A. Major, A. Crut, B. Gao, S.S. Lo, N. Del Fatti, F. Vallée, G.V. Hartland, Phys. Chem. Chem. Phys. 15 (2013) 4169–4176.
[108] K. Yu, T.A. Major, D. Chakraborty, M.S. Devadas, J.E. Sader, G.V. Hartland, Nano Lett. 15 (2015) 3964–3970.
[109] T. Devkota, D. Chakraborty, K. Yu, G. Beane, J.E. Sader, G.V. Hartland, Phys. Chem. Chem. Phys. 20 (2018) 17687–17693.
[110] J. Olson, S. Dominguez-Medina, A. Hoggard, L.-Y. Wang, W.-S. Chang, S. Link, Chem. Soc. Rev. 44 (2015) 40–57.
[111] T.A. Major, S.S. Lo, K. Yu, G.V. Hartland, J. Phys. Chem. Lett. 5 (2014) 866–874.
[112] V. Juvé, M.F. Cardinal, A. Lombardi, A. Crut, P. Maioli, J. Pérez-Juste, L.M. Liz-Marzán, N. Del Fatti, F. Vallée, Nano Lett. 13 (2013) 2234–2240.
[113] A. Lombardi, M.P. Grzelczak, A. Crut, P. Maioli, I. Pastoriza-Santos, L.M. Liz-Marzán, N. Del Fatti, F. Vallée, ACS Nano 7 (2013) 2522–2531.
[114] B. Foerster, A. Joplin, K. Kaefer, S. Celiksoy, S. Link, C. Sönnichsen, ACS Nano 11 (2017) 2886–2893.
[115] G. Beane, T. Devkota, B.S. Brown, G.V. Hartland, Rep. Prog. Phys. 82 (2019) 16401.
[116] D. Chakraborty, G.V. Hartland, M. Pelton, J.E. Sader, J. Phys. Chem. C 122 (2018) 13347–13353.
[117] R. Marty, A. Arbouet, C. Girard, A. Mlayah, V. Paillard, V.K. Lin, S.L. Teo, S. Tripathy, Nano Lett. 11 (2011) 3301–3306.
[118] J. Fedou, S. Viarbitskaya, R. Marty, J. Sharma, V. Paillard, E. Dujardin, A. Arbouet, Phys. Chem. Chem. Phys. 15 (2013) 4205–4213.
[119] A.D. O'Connell, M. Hofheinz, M. Ansmann, R.C. Bialczak, M. Lenander, E. Lucero, M. Neeley, D. Sank, H. Wang, M. Weides, et al., Nature 464 (2010) 697–703.
[120] J.D. Teufel, T. Donner, D. Li, J.W. Harlow, M.S. Allman, K. Cicak, A.J. Sirois, J.D. Whittaker, K.W. Lehnert, R.W. Simmonds, Nature 475 (2011) 359–363.
[121] S. Atta, F.E. Celik, L. Fabris, Faraday Discuss. 214 (2019) 341–351.
[122] Y.J. Jang, K. Chung, J.S. Lee, C.H. Choi, J.W. Lim, D.H. Kim, ACS Photonics 5 (2018) 4711–4723.
[123] L. Mascaretti, A. Dutta, Š. Kment, V.M. Shalaev, A. Boltasseva, R. Zbořil, A. Naldoni,Adv. Mater. (2019), 1805513.
[124] J.S. DuChene, G. Tagliabue, A.J. Welch, W.-H. Cheng, H.A. Atwater, Nano Lett. 18 (2018) 2545–2550.
[125] L. Weng, H. Zhang, A.O. Govorov, M. Ouyang, Nat. Commun. 5 (2014) 4792.
[126] S. Sarina, E. Jaatinen, Q. Xiao, Y.M. Huang, P. Christopher, J.C. Zhao, H.Y. Zhu, J. Phys. Chem. Lett. 8 (2017) 2526–2534.
[127] J. Huang, B. de Nijs, S. Cormier, K. Sokolowski, D.-B. Grys, C.A. Readman, S.J. Barrow, O.A. Scherman, J.J. Baumberg, Faraday Discuss. 214 (2019) 455–463.
[128] G. Tagliabue, J.S. DuChene, M. Abdellah, A. Habib, Y. Hattori, K. Zheng, S.E. Canton, D.J. Gosztola, W.-H. Cheng, R. Sundararaman, J. Sa, H.A. Atwater, arXiv: 1810.04238, 2018.

**Lucas V. Besteiro** is a joint Postdoctoral Fellow at the Institute of Fundamental and Frontier Sciences (UESTC, China) and the center Énergie, Matériaux et Télécommunications (INRS, Canada). His previous postdoctoral experience, at Ohio University, was preceded by his Ph.D. research at University of Santiago de Compostela, Spain. His research interests extend within Theoretical Nanophotonics and Material Science, with a focus on the computational modelling of plasmonic nanostructures for both fundamental and applied research.

**Peng Yu** is currently a group leader of plasmonic nanophotonics in the group of Prof. Alexander O. Govorov in the Institute of Fundamental and Frontier Sciences of University of Electronic Science and Technology of China. He obtained his bachelor's degree in Microelectronics in 2012 and master's degree in Electronic Information Materials and Components in 2015. His current research interests focus on plasmonics, including plasmon-enhanced light-harvesting and -emitting devices.

**Zhiming Wang** is currently a professor in the Institute of Fundamental and Frontier Sciences of University of Electronic Science and Technology of China. He obtained his bachelor's degree in Applied Physics in 1992, master's degree in Semiconductor Physics in 1995, and his Ph.D. degree in Condensed Matter Physics in 1998. He did postdoctoral studies in Paul-Drude-Institute for Solid State Electronics, Berlin, Germany in 2000. His current research interests focus on epitaxial crystal growth, molecular beam epitaxy, quantum dots, surfaces, interfaces, nanostructures, nanoscience, and nanotechnology.

**Alexander Holleitner**'s research is on photonic and non-equilibrium optoelectronic phenomena with particular emphasis on nanoscale and quantum materials as well as devices ranging from topological systems to atom-scale 2D materials. It covers fundamental quantum transport processes up to ultrafast charge and heat dynamics for photovoltaic and information technology applications. In 2007, he joined the Walter Schottky Institut and the Physics Department as a professor of the Technical University of Munich (TUM). He is a co-founder and head of the Center for Nanotechnology and Nanomaterials (ZNN) at TUM.

**Professor Hartland** joined the University of Notre Dame in 1994 after completing a Ph. D. in Chemistry at UCLA in 1991, and performing postdoctoral studies at the University of Pennsylvania. His research interests are in applying novel spectroscopy techniques to study the dynamics of single nanostructures in order to understand the energy relaxation processes in these materials, and how they interact with their environment. Prof. Hartland is a Fellow of the *American Association for the Advancement of Science*, the *American Chemical Society*, and the *Royal Society of Chemistry*. He is currently a Senior Editor for the *Journal of Physical Chemistry*.

**Gary P. Wiederrecht** is a Senior Scientist and Group Leader of the Nanophotonics & Biofunctional Structures Group in the Nanoscience & Technology Division at Argonne National Laboratory. He received a B.S. degree in chemistry from UC Berkeley in 1987 and a Ph.D. in physical chemistry from MIT in 1992. He is a Fellow of the American Physical Society. His research interests center on the photochemistry and photophysics of hybrid nanostructures, photochemical energy conversion, quantum optics, biomimetic materials, and the ultrafast optical responses of nanoparticles and nanoparticle assemblies.

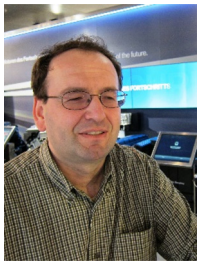

**Alexander O. Govorov** is a Professor of Physics at University of Electronic Science and Technology of China and a Distinguished Professor of Theoretical Physics at Ohio University, United States. His research focuses on the theory of optical and electronic properties of nanostructures and bioassemblies. His theoretical predictions have motivated experiments and have been implemented in many research labs worldwide. Dr. Govorov is the author of more than 250 papers. He is a Fellow of the American Physical Society and the recipient of several international awards including the Bessel Research Award (A. v. Humboldt Foundation), the Walton Visitor Award (Ireland), etc.